Publications of the Astronomical Society of the Pacific, 136:114201 (26pp), 2024 November https://doi.org/10.1088/1538-3873/ad8265

Searching for Gravitational Wave Optical Counterparts with the Zwicky Transient Facility: Summary of O4a

Tomás Ahumada[1,34], Shreya Anand[1,34], Michael W. Coughlin[2], Vaidehi Gupta[2,3], Mansi M. Kasliwal[1], Viraj R. Karambelkar[1], Robert D. Stein[1], Gaurav Waratkar[4], Vishwajeet Swain[4], Theophile Jegou du Laz[1], Akash Anumarlapudi[5], Igor Andreoni[6,7,8,35], Mattia Bulla[9,10,11], Gokul P. Srinivasaragavan[7], Andrew Toivonen[2], Avery Wold[12], Eric C. Bellm[13], S. Bradley Cenko[6,8], David L. Kaplan[5], Jesper Sollerman[14], Varun Bhalerao[4], Daniel Perley[15], Anirudh Salgundi[4], Aswin Suresh[4], K-Ryan Hinds[15], Simeon Reusch[16], Jannis Necker[16], David O. Cook[12], Natalya Pletskova[17], Leo P. Singer[8], Smaranika Banerjee[14], Tyler Barna[2], Christopher M. Copperwheat[18], Brian Healy[2], R. Weizmann Kiendrebeogo[2,19,20], Harsh Kumar[21,22], Ravi Kumar[23], Marianna Pezzella[24], Ana Sagués-Carracedo[25], Niharika Sravan[17], Joshua S. Bloom[26,27], Tracy X. Chen[12], Matthew Graham[28], George Helou[12], Russ R. Laher[12], Ashish A. Mahabal[1,29], Josiah Purdum[30], G. C. Anupama[31], Sudhanshu Barway[31], Judhajeet Basu[31], Dhananjay Raman[32], and Tamojeet Roychowdhury[33]

[1] Division of Physics, Mathematics and Astronomy, California Institute of Technology, Pasadena, CA 91125, USA
[2] School of Physics and Astronomy, University of Minnesota, Minneapolis, MN 55455, USA
[3] Department of Physics, Indian Institute of Technology Kharagpur, West Bengal, 721302, India
[4] Department of Physics, Indian Institute of Technology Bombay, Powai, 400076, India
[5] Department of Physics, University of Wisconsin-Milwaukee, P.O. Box 413, Milwaukee, WI 53201, USA
[6] Joint Space-Science Institute, University of Maryland, College Park, MD 20742, USA
[7] Department of Astronomy, University of Maryland, College Park, MD 20742, USA
[8] Astrophysics Science Division, NASA Goddard Space Flight Center, MC 661, Greenbelt, MD 20771, USA
[9] Department of Physics and Earth Science, University of Ferrara, via Saragat 1, I-44122 Ferrara, Italy
[10] INFN, Sezione di Ferrara, via Saragat 1, I-44122 Ferrara, Italy
[11] INAF, Osservatorio Astronomico d'Abruzzo, via Mentore Maggini snc, 64100 Teramo, Italy
[12] IPAC, California Institute of Technology, 1200 E. California Blvd, Pasadena, CA 91125, USA
[13] DIRAC Institute, Department of Astronomy, University of Washington, 3910 15th Avenue NE, Seattle, WA 98195, USA
[14] The Oskar Klein Centre, Department of Astronomy, Albanova, Stockholm University, SE-106 91 Stockholm, Sweden
[15] Astrophysics Research Institute, Liverpool John Moores University, IC2, Liverpool Science Park, 146 Brownlow Hill, Liverpool L3 5RF, UK
[16] Deutsches Elektronen-Synchrotron DESY, Platanenallee 6, 15738 Zeuthen, Germany
[17] Department of Physics, Drexel University, Philadelphia, PA 19104, USA
[18] Astrophysics Research Institute, IC2, Liverpool Science Park, 146 Brownlow Hill, Liverpool L3 5RF, UK
[19] Laboratoire de Physique et de Chimie de l'Environnement, Université Joseph KI-ZERBO, Ouagadougou, Burkina Faso
[20] Artemis, Observatoire de la Côte d'Azur, Université Côte d'Azur, Boulevard de l'Observatoire, F-06304 Nice, France
[21] Department of Physics, Indian Institute of Technology Bombay, Powai-400076, India
[22] Center for Astrophysics, Harvard & Smithsonian, USA
[23] Department of Aerospace Engineering, Indian Institute of Technology Bombay, Powai, 400 076, India
[24] Embry-Riddle Aeronautical University, Daytona Beach, Florida, USA
[25] The Oskar Klein Centre, Department of Physics, Stockholm University, AlbaNova, SE-106 91 Stockholm, Sweden
[26] Department of Astronomy, University of California, Berkeley, CA 94720, USA
[27] Lawrence Berkeley National Laboratory, 1 Cyclotron Road, MS 50B-4206, Berkeley, CA 94720, USA
[28] California Institute of Technology, 1200 E. California Blvd, Pasadena, CA 91125, USA
[29] Center for Data Driven Discovery, California Institute of Technology, Pasadena, CA 91125, USA
[30] Caltech Optical Observatories, California Institute of Technology, Pasadena, CA 91125, USA
[31] Indian Institute of Astrophysics, 2nd Block 100 Feet Rd, Koramangala Bangalore, 560034, India
[32] Department of Computer Science and Engineering, Indian Institute of Technology Bombay, Powai, 400076, India
[33] Department of Electrical Engineering, Indian Institute of Technology Bombay, Powai, 400076, India
Received 2024 June 6; accepted 2024 October 1; published 2024 November 8

Abstract

During the first half of the fourth observing run (O4a) of the International Gravitational Wave Network, the Zwicky Transient Facility (ZTF) conducted a systematic search for kilonova (KN) counterparts to binary neutron star

[34] These authors contributed equally.
[35] Neil Gehrels Fellow.

(BNS) and neutron star–black hole (NSBH) merger candidates. Here, we present a comprehensive study of the five high-significance (False Alarm Rate less than 1 yr^{-1}) BNS and NSBH candidates in O4a. Our follow-up campaigns relied on both target-of-opportunity observations and re-weighting of the nominal survey schedule to maximize coverage. We describe the toolkit we have been developing, `Fritz`, an instance of *SkyPortal*, instrumental in coordinating and managing our telescope scheduling, candidate vetting, and follow-up observations through a user-friendly interface. ZTF covered a total of 2841 deg^2 within the skymaps of the high-significance GW events, reaching a median depth of $g \approx 20.2$ mag. We circulated 15 candidates, but found no viable KN counterpart to any of the GW events. Based on the ZTF non-detections of the high-significance events in O4a, we used a Bayesian approach, `nimbus`, to quantify the posterior probability of KN model parameters that are consistent with our non-detections. Our analysis favors KNe with initial absolute magnitude fainter than -16 mag. The joint posterior probability of a GW170817-like KN associated with all our O4a follow-ups was 64%. Additionally, we use a survey simulation software, `simsurvey`, to determine that our combined filtered efficiency to detect a GW170817-like KN is 36%, when considering the 5 confirmed astrophysical events in O3 (1 BNS and 4 NSBH events), along with our O4a follow-ups. Following Kasliwal et al., we derived joint constraints on the underlying KN luminosity function based on our O3 and O4a follow-ups, determining that no more than 76% of KNe fading at 1 mag day^{-1} can peak at a magnitude brighter than -17.5 mag.

Unified Astronomy Thesaurus concepts: Gravitational waves (678); Transient detection (1957); Optical observation (1169); Explosive nucleosynthesis (503); Compact binary stars (283); Compact objects (288)

1. Introduction

The increased sensitivity of gravitational-wave detector networks have enabled unprecedented discoveries of compact binary mergers in the last decade. The International Gravitational Wave Network (IGWN) detected 102 binary black hole (BBH) mergers, 2 binary neutron star (BNS) mergers and 4 neutron star–black hole (NSBH) mergers between 2015 and 2020 during the first three observing runs (Abbott et al. 2023a). The growing population of BBH mergers have challenged the existence of both the upper and lower black hole mass gaps (Abbott et al. 2020b, 2020c), and have revealed a unique population of low-spin black holes (Tiwari et al. 2018). The second observing run of IGWN marked the discovery of GW170817, the very first GW signal from a BNS merger system (Abbott et al. 2017), with its short gamma-ray burst (GRB) counterpart (Abbott et al. 2017; Goldstein et al. 2017), panchromatic afterglow (Haggard et al. 2017; Hallinan et al. 2017; Margutti et al. 2017; Troja et al. 2017; Mooley et al. 2018; Pozanenko et al. 2018; Makhathini et al. 2021; Balasubramanian et al. 2022; Mooley et al. 2022), and optical/IR kilonova (KN) (Coulter et al. 2017; Drout et al. 2017; Evans et al. 2017; Kasen et al. 2017; Kasliwal et al. 2017; Lipunov et al. 2017; Soares-Santos et al. 2017; Utsumi et al. 2017; Valenti et al. 2017; Arcavi 2018; Kasliwal et al. 2022). IGWN's third observing run yielded another BNS merger (Abbott et al. 2020a) along with the first ever detections of NSBH mergers (Abbott et al. 2020, 2021, 2023a), though no electromagnetic counterpart was found for any of these events.

Many collaborations such as the Zwicky Transient Facility (ZTF; Bellm et al. 2019a; Graham et al. 2019; Dekany et al. 2020), Electromagnetic counterparts of Gravitational wave sources at the Very Large Telescope (ENGRAVE; Levan 2020), Global Rapid Advanced Network Devoted to the Multi-messenger Addicts (GRANDMA; Antier et al. 2020), Gravitational-wave Optical Transient Observer (GOTO; Gompertz et al. 2020), All Sky Automated Survey for SuperNovae (Shappee et al. 2014), Asteroid Terrestrial Last Alert System (ATLAS; Tonry et al. 2018), Panoramic Survey Telescope and Rapid Response System (Pan-STARRS; Chambers et al. 2016), MASTER-Net (Lipunov et al. 2017), Searches after Gravitational Waves Using ARizona Observatories (Lundquist et al. 2019), Gravitational-wave Electromagnetic Counterpart Korean Observatory (Paek et al. 2024), the Dark Energy Survey Gravitational Wave Collaboration (DES-GW; Soares-Santos et al. 2017), Global Relay of Observatories Watching Transients Happen (GROWTH[36]), Burst Optical Observer and Transient Exploring System (Hu et al. 2023), KM3Net[37] and VINROUGE[38] undertook targeted efforts during IGWN's third observing run (O3) to identify any associated electromagnetic counterparts. However, despite extensive tiling and galaxy-targeted searches, no EM counterparts were found (Andreoni et al. 2019; Coughlin et al. 2019; Goldstein et al. 2019; Andreoni et al. 2020a; Antier et al. 2020; Kasliwal et al. 2020; Morgan et al. 2020; Vieira et al. 2020; Alexander et al. 2021; de Wet et al. 2021; Kilpatrick et al. 2021; Thakur et al. 2021; Dobie et al. 2022; Rastinejad et al. 2022; Tucker et al. 2022). Among the 6 BNS and 9 NSBH merger candidates announced in O3, only 1 BNS merger (GW190425) and 4 NSBH merger candidates (GW190426, GW190814, GW200105, and GW200115) passed the False Alarm Rate (FAR) threshold for inclusion in the Gravitational Wave

[36] http://growth.caltech.edu/
[37] https://www.km3net.org/
[38] https://www.star.le.ac.uk/nrt3/VINROUGE/

Transient Catalog (GWTC-3; Abbott et al. 2023a) as high-confidence signals, rendering the remainder of the candidates as subthreshold astrophysical events or noise sources. Nevertheless, the dearth of BNS mergers during O3 revised the projected astrophysical rate of BNS mergers to 50–440 $\mathrm{Gpc^{-3}\,yr^{-1}}$ (Abbott et al. 2023b), assuming uniform mass and spin distributions, and that the merger rate is constant in comoving volume out to $z = 0.15$.

IGWN's fourth observing run (O4) commenced on 2023 May 24 and paused for a commissioning break on 2024 January 15, marking the end of the first half of the observing run (O4a). Based on the sensitivity of the LIGO and Virgo detectors, observing scenarios studies (Weizmann Kiendrebeogo et al. 2023) predicted that 36^{+49}_{-22} BNS and 6^{+11}_{-5} NSBH mergers would be detected at the public alert release threshold during the first year of O4, which is consistent with the number of potential NS merger candidates (including those of low significance, there are 27 events with `HasNS` >0.5 and FAR better than 1 per week) released thus far during O4a (lasting 8 months). These estimates included the Virgo detector as a part of the GW network, whose sensitivity was projected to be between 40 and 80 Mpc. Virgo has now joined the O4 run since 2024 April at a rough sensitivity of ≈50 Mpc. The rates are driven by the LIGO interferometers, and the inclusion of Virgo does not affect the predicted rates dramatically; however, it results in better localized NS mergers.

The ZTF, mounted on the Samuel Oschin 48 inch Telescope at Palomar Observatory, is a public-private project that routinely acquires 30 s images in the *g*-, *r*- and *i*-band, covering the entire available northern night-sky every two nights. Due to its cadence, ZTF has one of the most complete records of the contemporary dynamic sky. This capability enables the detection of transients at the early stages of their active phase. The use of ZTF for GRB and GW optical counterparts searches, over thousands of square degrees (Kasliwal et al. 2020; Ahumada et al. 2022) has allowed for the discovery of rare GRB afterglows: the shortest burst associated to a collapsar (Ahumada et al. 2021), an orphan afterglow during O3 (Perley et al. 2024), and the afterglow of one of the brightest GRBs (Srinivasaragavan et al. 2024). We used ZTF (more details in Section 2) to conduct wide-field tiling searches of 5 high-significance GW candidates (S230518h, S230529ay, S230627c, S230731an, and S231113bw) aiming to detect an EM counterpart. For completeness, we also include 5 other (lower significance) GW candidates for which ZTF has coverage, in the Appendix (see Section B).

In this paper, we start in Section 2 describing how ZTF is used to perform searches for EM counterparts to GW sources during O4a. We outline the triggering mechanisms for ZTF in Section 2.4. In Section 3 we give a description of the analysis pipelines and candidate filtering criteria, alongside the new and improved software toolkit for enabling counterpart discovery. In Section 4 we provide details of the GW events we triggered ZTF on, and in Section 5 we determine the efficiency of our efforts, and derive constraints to the KN luminosity function. We finalize the paper with conclusions in Section 6.

2. Zwicky Transient Facility Follow-up

In this section, we describe the ZTF triggering criteria for GW events during O4a. We start by describing the IGWN public data products that were used to evaluate the relevance of an event, and we continue describing the ZTF triggering criteria and the methods used to trigger and schedule ZTF observations.

2.1. GW Metrics

The strain data of the GW events is analyzed in real time by different pipelines. Some pipelines such as GSTLal (Cannon et al. 2021), PyCBC Live (Nitz et al. 2018), the Multi-Band Template Analysis (Adams et al. 2016), and the Summed Parallel Infinite Impulse Response (Guo et al. 2018) match the signal to a template bank of compact binaries coalescences (CBCs), while others, such as cWB (Klimenko et al. 2008) and oLIB (Lynch et al. 2017), search for bursts of power in the GW spectra. These pipelines include the FAR of the event in their public data products, as well as an initial 3D localization map produced by BAYESTAR (Singer & Price 2016). In addition to this, pipelines searching for CBCs release metrics related to the template matching results, indicating the probability of a merger to have a BBH, BNS, NSBH, or Terrestrial origin in the initial GCN announcement (p_{BBH}, p_{BNS}, p_{NSBH}, and $p_{\mathrm{Terrestrial}}$ respectively). This first online pipeline analysis is followed by a machine-learning-based inference (Chatterjee et al. 2020), that sheds light onto whether at least one NS was part of the binary (`HasNS`), whether the merger is likely to leave a non-zero remnant behind (`HasRemnant`), or if it involves an object in the 3–5 $M_{\odot}$ mass gap (`HasMassGap`).

2.2. Triggering Criteria

During O3, ZTF conducted a search for optical counterparts for all observable BNS, NSBH, and MassGap events (Kasliwal et al. 2020). These criteria resulted in 13 campaigns, spanning GW events with FARs between 10^{-25} and 24 $\mathrm{yr^{-1}}$. The offline GW analysis post-O3 confirmed only five of these candidates as likely CBCs (GW190425, GW190426, GW190814, GW200105, and GW200115), while retracting all other events (Abbott et al. 2023b). During O4, we decided to take the FAR and other low-latency GW parameters into consideration at the time of triggering ZTF observations. Given that the FAR depends on the template bank of each pipeline, there are usually discrepancies between the different pipelines that have to be considered case by case. Generally, the ZTF trigger criteri

Table 1
Summary of ZTF Observations and GW Properties of the 5 GW Events Selected and Analyzed in this Paper

Trigger	Strategy	FAR (yr^{-1})	p_{BNS}	p_{NSBH} prob.	`HasNS` prob.	`HasRemnant` prob.	`HasMassGap` prob.	Distance (Mpc)	Covered prob.	Area Covered (deg^2)	g-band Depth (AB mag)	Latency (hr)
S230518h	No coverage	0.01	0.0	0.86	1.0	0.0	0.0	204	…	…	…	…
GW230529	Re-weighting	0.006	0.31	0.62	0.98	0.07	0.73	197	7%	2425	20.6	10
S230627c	ToO	0.01	0.0	0.49	0.0	0.0	0.14	291	74%	72	21.03	2.2
S230731an	Re-weighting	0.01	0.0	0.18	0.0	0.0	0.0	1001	3%	43	18.7	12.4
S231113bw	Re-weighting	0.42	0.0	0.17	0.0	0.0	0.02	1186	11%	301	21.17	7.7

Note. We required their FAR to be less than 1 yr^{-1}, and one of the following: $p_{BNS} > 0.1$, $p_{NSBH} > 0.1$, or `HasNS` > 0.1. We quote other quantities intrinsic to the GW event, such as the mean distance to the merger, the `HasRemnant`, and the `HasMassGap` parameters. For each event we summarize the coverage, depth and latency for the ZTF observations. We include the events with FAR > 1 yr^{-1} in Table 2 in the Appendix B. To determine the areal coverage and the enclosed skymap probability observed by ZTF, we require at least two ZTF observations in a given region.

a prioritized events with FAR $< 1\,yr^{-1}$ and one of the following: `HasNS` > 0.1, `pBNS` > 0.1, or `pNSBH` > 0.1 to avoid BBHs and terrestrial events. These criteria were intended to address the substantial volume of low-significance events, rather than serving as rigid criteria. During O4a, there were 150 events with `pBNS` > 0.1 or `pNSBH` > 0.1, however, only 5 of these had false alarm rates less than $1\,yr^{-1}$. We used ZTF to follow-up all 5 of them (see Table 1 and Section 4).

2.3. ZTF Strategies

In O4, ZTF developed two observing strategies for GW events that were identified as high confidence (FAR $< 1\,yr^{-1}$, and `HasNS` > 0.1 or $p_{BNS} > 0.1$ or $p_{NSBH} > 0.1$). The first strategy relied on interrupting the nightly schedule of ZTF through a Target of Opportunity (ToO) trigger, in order to cover the GW region with exposures longer than the nominal 30 s survey exposures. This strategy allowed us to conduct observations with exposures up to 300 s, and was limited to high confidence and well localized events (i.e., events with their 50% error region contained to less than 5800 deg^2, and observable from Palomar). Our nominal ToO strategy covers the skymaps in multiple filters during night 0, night 1, night 2, and night 7. To prepare for O4, ZTF developed a set of deep reference images of the ZTF grid, which allowed for robust image subtraction of our deeper ToO observations. The median limiting magnitude of these deeper references is 23.0 mag for the i-band, and 23.5 mag for g- and r-bands.

The second strategy relies on the deliberate rearrangement of the ZTF fields that are part of the regular survey operations. The nightly ZTF schedule is optimized for the discovery and characterization of the dynamic optical sky, while systematically observing different areas of the sky (Bellm et al. 2019b). During O3, we relied on serendipitous ZTF coverage of GW skymaps for low significance or poorly localized events. However, for O4, we developed an alternative approach, referred to as "re-weighting" that makes use of the nominal 30 s exposures of the ZTF public survey and constructs a re-weighted schedule, prioritizing the ZTF fields that overlap with the GW localization area. This strategy conducts observations during the first and second night after a trigger.

2.4. Triggering ZTF Observations

The scheduling of ZTF observations to tile and cover GW error regions can be done through multiple avenues, and the bulk of our triggers were managed through `Fritz`, an instance of *SkyPortal* (van der Walt et al. 2019; Coughlin et al. 2023). *SkyPortal* combines the functionalities of two separate tools: the GROWTH Marshal (Kasliwal et al. 2019) and the GROWTH Target of Opportunity Marshal (Coughlin et al. 2019), while providing additional functionalities that further automate the EMGW follow-up process. While the GROWTH Marshal offered the ability to save candidates from different discovery streams and assign follow-up, the GROWTH ToO Marshal allowed for the interaction with skymaps. As a result, *SkyPortal* provides a user-friendly tool that facilitates the management and exploration of astronomical data, allowing one to schedule observations and easily retrieve data associated to a skymap. Particularly, `Fritz` is optimized to interact with ZTF, as it retrieves data from the ZTF database `Kowalski` (Duev et al. 2019), displays light-curves and spectra of ZTF objects, and enables interaction with multi-messenger events, such as GWs, among other key features. `Fritz` continuously listens to the GCN stream of alerts (Singer & Racusin 2023) and generates an interactive GCN event page for each new alert, including for GWs, GRBs, and neutrino alerts (see Figure 1). Information intrinsic to each GCN, such as p_{BNS} or `HasNS`, is readily accessible through this page. Additionally, `Fritz` facilitates the management and execution of ZTF observation plans (as well as for other facilities, such as DECam, WINTER, Palomar Gattini IR, and the GROWTH-

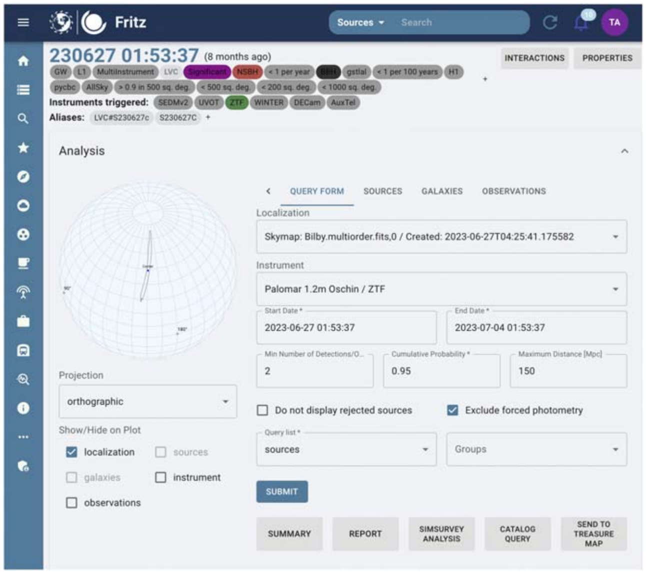

Figure 1. The `Fritz` page for a GW event displays information in tags located below the date of the event. In the Properties tab, it presents information originally available in the GCN. The page exhibits the most up-to-date information available, as well as the history of changes circulated through GCNs.

India Telescope). As a new event comes in and is added to `Fritz`, a default ZTF observing plan is created with `gwemopt`, a schedule optimizer originally developed to handle GW skymaps (Coughlin et al. 2018). The default `gwemopt` plan consists of three visits per field, each lasting 300 s, organized in blocks of *g*-, *r*-, and *g*-band observations to minimize time lost to filter exchange. However, this default strategy can be modified by requesting a new observing plan with adjusted exposure times and filter sequences, or by targeting a subsection of the GW skymap. By adjusting the observing plan ZTF could be used to cover a larger portion of the sky: as a reference three 300 s visits per field cover 1128 deg^2 in 6 hr, while two 120 s visits per field cover 4230 deg^2 in the same amount of time. For each observing plan, `Fritz` additionally displays the tiling of the region in a dynamic skymap, and a summary of the plan including the duration of the observations, the areal coverage, and the probability enclosed. The finalized plan can be submitted to the ZTF queue through `Fritz`.

For events that required a re-organization and re-weighting of the nominal 30 s ZTF observations, the procedure requires communication with the ZTF scheduler (Bellm et al. 2019b).[39] This was accomplished by sending fields and their integrated probabilities from the GW skymap to the ZTF scheduler through an integrated API in `Fritz`. Once the fields are received, the scheduler assigns 30 s epochs in *g*-, *r*-, and *i*-bands to the highest probability fields.

Additionally, we developed an open source Simple Nodal Interface for Planning Electromagnetic Reconnaissance of Gravitational Waves (`SniperGW`),[40] a programmatic avenue to access the ZTF scheduler, as a back-up that can be run on a laptop. `SniperGW` directly downloads maps from `GraceDB`, uses `gwemopt` to generate the schedules, and communicates directly with the ZTF scheduler via API. This serves as an "offline" method for us to submit schedules in real-time in case the `Fritz` database is down, and also allows more flexibility to customize schedules if needed.

3. Analysis Pipelines

The ZTF pipeline (Masci et al. 2019), running at the Infrared Processing and Analysis Center (IPAC[41]), reduces, calibrates and performs image subtraction in near real time. Any 5σ flux deviation from the reference image issues an alert (Patterson et al. 2019), containing metadata of the transient, including its light-curve history, real-bogus score (Duev et al. 2019), and cross-matches with Pan-STARRS (Chambers et al. 2016), among other useful quantities. These alerts are issued to brokers all around the globe, such as ALeRCE (Förster et al. 2016), AMPEL (Nordin et al. 2019), ANTARES (Saha et al. 2014), Lasair (Smith et al. 2019), Fink (Möller et al. 2020), and Pitt-Google.[42] Some of these brokers maintain their own databases with ZTF data, allowing users to manage and filter the alerts in order to recover transients of interest.

3.1. Transient Searches: Automatic Filtering

Throughout O4a, we relied on four methods to select transients from the ZTF stream: `Fritz`, `nuztf`, `emgwcave`, and the ZTF REaltime Search and Triggering (`ZTFReST`; Andreoni et al. 2021). Some of these tools were used during O3, and build on developments following the past IGWN run. Each tool developed a unique alert filtering scheme, however, they have a common core:

1. *In the GW skymap.* The candidate is required to be inside the 95% contour of the latest and most up-to-date GW skymap.
2. *Positive subtraction.* We focus on sources that have brightened and have a positive residual after image subtraction.
3. *Real astrophysical sources.* ZTF has developed a machine learning (ML) model to identify sources that are created by ghosts or artifacts in the CCDs. The model was trained with known ZTF artifacts and it relies on a deep convolutional neural network (Duev et al. 2019).

[39] https://github.com/ZwickyTransientFacility/ztf_sim

[40] https://github.com/robertdstein/snipergw

[41] https://www.ipac.caltech.edu/

[42] https://pitt-broker.readthedocs.io/en/latest/

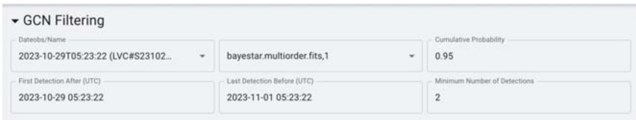

Figure 2. A snapshot illustrating the spatial and temporal constraints set on `Fritz` for transients selection. This feature is used to refine the candidate query, limiting it to a specific region (Cumulative Probability) on a skymap within a designated time-frame.

Generally, sources with Real-Bogus score >0.3 are considered to be of astrophysical origin.

4. *Avoid known point sources*. To avoid contamination from stars, we enforce transients to be greater than 3 arcsec from any point source in the PS1 catalog based on Tachibana & Miller (2018).
5. *Minimum of two detections*. To reject slow moving solar system objects and cosmic rays, we enforce a minimum of two detections separated by at least 15 minutes.
6. *Far from a bright star*. It is well known that bright sources produce artifacts and ghosts, thus we require a minimum distance of $>20''$ from sources with $m_{\mathrm{AB}} < 15$ mag.
7. *First detection after the GW event.* KNe and relativistic afterglows are only expected after the merger, thus we filter out sources with activity previous to the GW event.

The majority of the analysis was carried out on `Fritz`: from planning the observing strategy, to the selection of candidates, and the orchestration of their follow-up. For the selection of candidates, we set in place *two* `MongoDB` filters to interact with `Kowalski`, the ZTF database, via `Fritz`. Both filters followed the points established above, and while the `EM+GW` filter aims to serve as a thorough census of all the extragalactic sources spatially and temporally consistent with a GW event, the `EM+GW PtAu` filter was designed to recover transients within 150 kpc of projected distance from a galaxy, either in the Census of the Local Universe (CLU; Cook et al. 2019) or in the NASA/IPAC Extragalactic Database—Local Volume Sample (NED-LVS; Cook et al. 2023) catalogs. A major development in O4a is the flexible candidate searches in different skymaps. We used to rely on offline cross-matching for each candidate, in order to determine at what credible level within the GW skymap each candidate was discovered. Now, the searches can be customized through `Fritz`, by selecting a skymap, a credible level, and a detection date, in order to retrieve the candidates that meet the selected criteria. This new feature allows us to easily determine which ZTF sources are inside a skymap, and it has been used to revise candidates when a newly updated GW skymap is circulated (see Figure 2).

`Fritz` was intended to provide a stable and reliable way to access, filter, visualize, and interact with ZTF data. It was optimized to cater to multiple science cases with a trade-off in flexibility. Although alert filters can easily be modified, real-time fine-tuning adjustments are difficult to implement. For this reason, we have other software stacks that enable independent queries to `AMPEL` and Kowalski, the ZTF databases. Having multiple tools analyzing the ZTF data stream allows us to be meticulously thorough, to increase our completeness, and to understand how the different alert filters affect our results. In this section we describe complementary methods used to filter ZTF alerts.

First, we conducted an independent search using the `nuztf`[43] `python` package (Stein et al. 2023), originally developed for the ZTF Neutrino Follow-Up Program (see Stein et al. 2023 for further details). `nuztf` uses the `AMPEL` framework to conduct candidate filtering (Nordin et al. 2019), and uses the `AMPEL` broker data archive to retrieve ZTF data at very low latency (Nordin et al. 2019). `AMPEL` provides a direct healpix API query that can return candidates within a given skymap. We perform cuts similar to those listed above to select candidates, and then perform automated cross-matching with various multi-wavelength catalogs to flag likely variable AGN or stars. `nuztf` can export candidates to `Fritz`, as well as produce summary PDFs for quick candidate scanning. `nuztf` uses ZTF observation logs from IPAC to calculate survey coverage of a skymap, accounting for chip gaps and any processing failures in each of the 64 ZTF quadrants.

The Kowalski database was queried independently through `emgwcave`,[44] a python-based script that retrieves candidates based on the cuts similar to the ones described above. emgwcave offers an extra layer of flexibility, as the queries can be easily modified. Similar to the `nuztf` searches, the candidates are cross-matched with multiple catalogs in order to identify AGNs and variable stars. The resulting outcomes are then exported to a PDF file and simultaneously pushed to `Fritz`.

Finally, we made use of the `ZTFReST` infrastructure (Andreoni et al. 2021). This open-source code allows the exploration of ZTF data, and the flagging of fast fading transients. `ZTFReST` derives the evolution of a given transient based on the photometry in the ZTF alerts and forced photometry (Yao et al. 2020). The ranking of transients considers factors such as the galactic latitude, the cross-match to multi-wavelength catalogs, and the magnitude evolution. `ZTFReST` highlights transients through a user-friendly `Slack`-bot that enables the scanning of candidates.

All candidates passing the automatic filter are submitted to the Transient Name Server (TNS[45]).

[43] https://github.com/desy-multimessenger/nuztf
[44] https://github.com/virajkaram/emgwcave
[45] https://www.wis-tns.org/

3.2. Transient Vetting: Source by Source—Humans in the Loop

Once a transient passes either of the filters set in place (`EM+GW` or `EM+GW PtAu`), it can be easily retrieved through `Fritz` where we have implemented an efficient spatial filter through Healpix Alchemy (Singer et al. 2022) that allow us to query transients in a given portion of a specific skymap. If a candidate passes any of the other offline filters (`nuztf`, `emgwcave`, or `ZTFReST`), it can easily be included in the main `Fritz` group and be analyzed using the `Fritz` capabilities. The `Fritz` interface allows one to easily modify the spatial query and retrieve ZTF transients at different credible levels, as seen in Figure 2. Each of the transients that pass our automatic filters and are inside the default 95% credible region of the GW map, is now visually inspected.

During O3, a key feature to discriminate candidates was the use of ZTF forced photometry (FP). Thanks to a number of modifications and improvements in the IPAC request and retrieval of FP products, `Fritz` has now integrated forced photometry capabilities. For each transient, there is the option to directly request FP from the `Fritz` source page, and additionally select the time window of interest, that could go back to the start of the survey. Similarly, `Fritz` has made use of the ATLAS FP service (Shingles et al. 2021), and it has implemented a similar system for data retrieval. For both services, the products include the flux information and its uncertainty. We set a threshold of 3σ for detections and we take this information into account when ruling out sources. We also download the ATLAS images associated with the forced photometry for further inspection.

The `Fritz` alert filters can retrieve additional information for the candidates, as they are ingested in the *Kowalski* database, they are also crossmatched with a number of surveys. Data from the Wide-Field Infrared Survey Explorer (WISE; Wright et al. 2010) and Milliquas (Flesch 2023) are retrieved and used to assess whether a source is associated to an active galactic nuclei (AGN): for WISE we use the $W1 - W2 > 0.6$ cut (Wright et al. 2010), while for Milliquas we require a quasar probability $p_{\rm QSO} < 0.8$. Since the WISE point-spread function (PSF) is around $6''$ (compared to ZTF's $1''$ PSF), additional human vetting is required to ensure the association to an AGN.

3.3. Transient Vetting: Assigning Follow-up

In many cases, the objects discovered in GW search campaigns require additional photometric and/or spectroscopic follow-up in order to discern the nature of the transients and determine whether they could be a viable EM counterpart. Objects passing the filtering criteria outlined in Sections 3.1 and 3.2 can be assigned external photometric and spectroscopic follow-up through `Fritz`. For example, we triggered the Spectral Energy Distribution Machine (SEDM; Blagorodnova et al. 2018; Rigault et al. 2019; Kim et al. 2022) for both spectroscopy and imaging and Las Cumbres Observatory (Brown et al. 2013) for imaging during our O4a GW search campaigns through `Fritz`. We triggered several other external photometric and spectroscopic facilities to photometrically monitor and classify transients found during our GW search campaigns; these facilities are described in Sections A.1 and A.2.

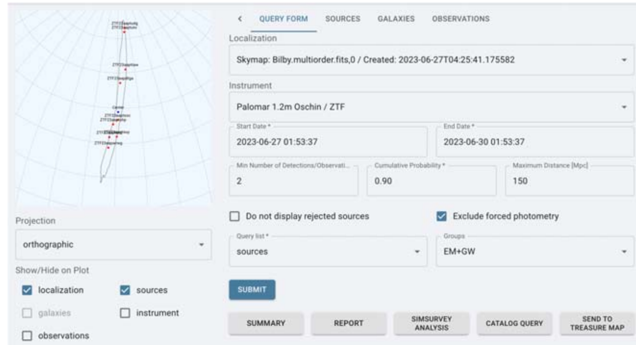

Figure 3. Snapshot of the GCN Analysis `Fritz` page. In this case, we display the sources within the 90% localization of the GW event S230627c passing the EM+GW filter in the corresponding GW skymap.

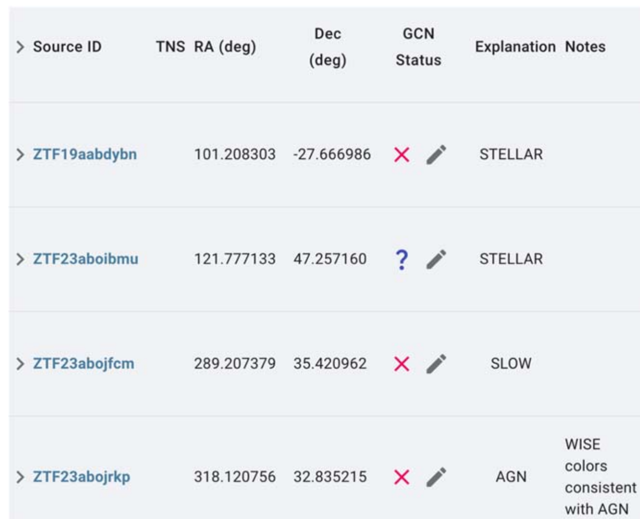

Source ID	TNS	RA (deg)	Dec (deg)	GCN Status	Explanation	Notes
ZTF19aabdybn		101.208303	-27.666986	✕	STELLAR	
ZTF23aboibmu		121.777133	47.257160	?	STELLAR	
ZTF23abojfcm		289.207379	35.420962	✕	SLOW	
ZTF23abojrkp		318.120756	32.835215	✕	AGN	WISE colors consistent with AGN

Figure 4. Snapshot of the GCN Analysis `Fritz` page showing the rejection criteria for candidates discovered within the 90% localization of S231029k.

After retrieving promising candidates within the GW localization (see Figure 3), we used in-built `Fritz` functionality to track the status of each candidate, a novelty during O4a. For each candidate, we can either highlight it, mark it as ambiguous, reject it, or flag it as a source that still needs to be vetted (see Figure 4). We can choose a reason for selection or rejection from a dropdown menu spanning the following categories:

1. `Local/Far`—based on the photometric/spectroscopic redshift of a potentially associated host galaxy, a candidate appears to be consistent with the GW distance, or too far to be associated with it.
2. `New/Old`—based on either alerts or forced photometry, a candidate that is temporally consistent with the GW event (i.e., the first alerts occur after the GW trigger time) or has a history of previous detections.
3. `Red`—based on either alerts or forced photometry a candidate exhibits red colors in its light curve ($g - r > 0.3$ mag), as expected for a KN.
4. `Fast/Slow`—based on either alerts or forced photometry, a candidate's light curve evolves more rapidly or slowly than 0.3 mag day^{-1} (the minimum decay rate expected for a KN-like transient; Andreoni et al. 2020b).
5. `Rock`—based on examination of image cutouts or light curve, a candidate is characterized as a moving object.
6. `Stellar`—a star lies within 2″ from the candidate position and/or the light curve has stellar-like variability.
7. `AGN`—a candidate's host galaxy exhibits WISE colors consistent with an AGN, it shows photometric variability, and/or it is spectroscopically classified as AGN.
8. `Bogus`—upon detailed examination of alert image PSFs, a candidate appears to be an image artifact.
9. `Specreject`—the spectrosopic classification of a candidate matches neither a GRB afterglow nor a KN.

Optionally, users can also leave a customized note on the candidate, providing additional information not captured in the dropdown menu. Since the selection/rejection tool is dynamic, users can update the status of a given candidate once additional information (such as forced photometry, or follow-up photometry/spectroscopy) has been obtained. One such example of the candidate selection/rejection tool is shown in Figure 4 for the GW event S231029k.

```
TITLE: GCN SUMMARY TEST OBS

SUBJECT: Follow-up on GCN Event 2023-05-21T05:30:43

DATE: 2023-05-31 22:45:46.066066

FROM:  theophile du laz at ... <theophile.dulaz@gmail.com>


on behalf of the EM+GW, report:


Observations:


Palomar 1.2m Oschin - ZTF:

We observed the localization region of LVC trigger 2023-05-21T05:30:43.000 UTC.  We obtained a total of 401 images
covering ztfg,ztfi,ztfr bands for a total of 13380 seconds. The observations covered 3048.1 square degrees beginning at
2023-05-21T05:32:51.999 (2 minutes after the burst trigger time) corresponding to ~29% of the probability enclosed in the
localization region.
The table below shows the photometry for each observation.
```

```
TITLE: EXAMPLE AUTO-GENERATED GCN CIRCULAR

SUBJECT: ZTF Follow-up of the GW event S230521k

DATE: 2024-01-22 21:33:04.877467

FROM:  Shreya Anand at ... <sanand@caltech.edu>


T. Ahumada (...), S. Anand (...)


on behalf of the EM+GW, report:


Found 10 sources in the event's localization, 9 of which have been rejected after characterization:

Sources:
+-------------+---------+----------+---------+-----------+-------------+
| id          | tns     |       ra |     dec | redshift  | comment     |
|-------------+---------+----------+---------+-----------+-------------|
| ZTF23aalcvpw | 2023jfp | 173.4715 | 29.1938 |           | bluer, host, |
+-------------+---------+----------+---------+-----------+-------------+

Rejected sources:
+-------------+-------+----------+---------+-----------+------------------------------------------------+
| id          | tns   |       ra |     dec | redshift  | comment                                        |
|-------------+-------+----------+---------+-----------+------------------------------------------------|
| ZTF23aalbwxx |       | 176.5481 | -0.9106 |           | redder, no host, rock within 30 arcsec         |
| ZTF23aalbypp |       | 179.2981 |  2.1502 |           | redder, no host, rock withi 10 arcsec          |
| ZTF23aalcoas |       | 176.3550 | -2.7421 |           | single band data, no host, rock within 10 arcsec |
| ZTF23aalcqpv |       | 175.8908 |  3.0439 |           | bluer, no host, rock within 10 arcsec          |
| ZTF23aalcqtk |       | 176.0103 |  6.2305 |           | single band data, no host, rock within 10arcsec |
| ZTF23aaldebi |       | 179.2978 |  2.1501 |           | single band data, no host, rock within 10arcsec |
| ZTF23aaldfpg |       | 177.7096 |  1.4222 |           | single band data, rock within 5 arcsec         |
| ZTF23aalbwua |       | 177.6670 | -0.3263 |           | redder, no host, rock within 10 arcsec         |
| ZTF23aaldgfi |       | 176.5482 | -0.9103 |           | single band data, no host, rock within 5 arcsec |
+-------------+-------+----------+---------+-----------+------------------------------------------------+
```

Figure 5. Two examples of auto-generated GCN circular text for the GW event S230521k. Top: a summary of the actual ZTF observations conducted. Bottom: selected and rejected candidates within the GW localization.

3.4. Transient Vetting: Dissemination of Candidates

The last step is to disseminate the details of our observations and final candidate selection via GCN circular to the broader astronomical community. Based on the status of candidates marked in the selection/rejection tool, they will be automatically sorted into separate table and displayed in the content of the GCN circular. Furthermore, `Fritz` generates a summary of the conducted ZTF observations, with probability and areal coverage within the requested time window, along with a detailed table of the ZTF photometry. Examples of auto-generated GCN circular text summarizing ZTF observations as well as tables with highlighted and rejected candidates are shown in Figure 5. This new, streamlined system for retrieving transients within the localization, tracking their status, and generating a GCN draft allowed for the timely circulation of interesting candidates discovered with ZTF to the rest of the multi-messenger astronomy (MMA) community. The ZTF fields and the coverage of the gravitational wave skymap is also made available through `Treasuremap` (Wyatt et al. 2020) to the community.

4. Summary of ZTF Triggers

In this section we describe the ZTF observations of 5 O4a GW events that had a probability of BNS or NSBH greater than 0.1 (see Table 1) and a FAR <1 yr^{-1}. In Appendix A we describe the observations of 5 additional GW events with FAR greater than 1 yr^{-1}. Of the events described in this section, only S230627c passed our criteria to trigger ToO observations. We obtained some serendipitous observations within the skymap of S230518h, but the updated skymap excluded the ZTF-observed regions. The remaining events (GW230529, S230731an, S231113bw) were observed using the re-weighting strategy (see Table 1).

4.1. S230518h

The first event detected during O4a was during the engineering run, on 2023 May 18th (Ligo Scientific Collaboration et al. 2023a). This event was a highly significant event (FAR of one per 100 yr) and was originally classified as a

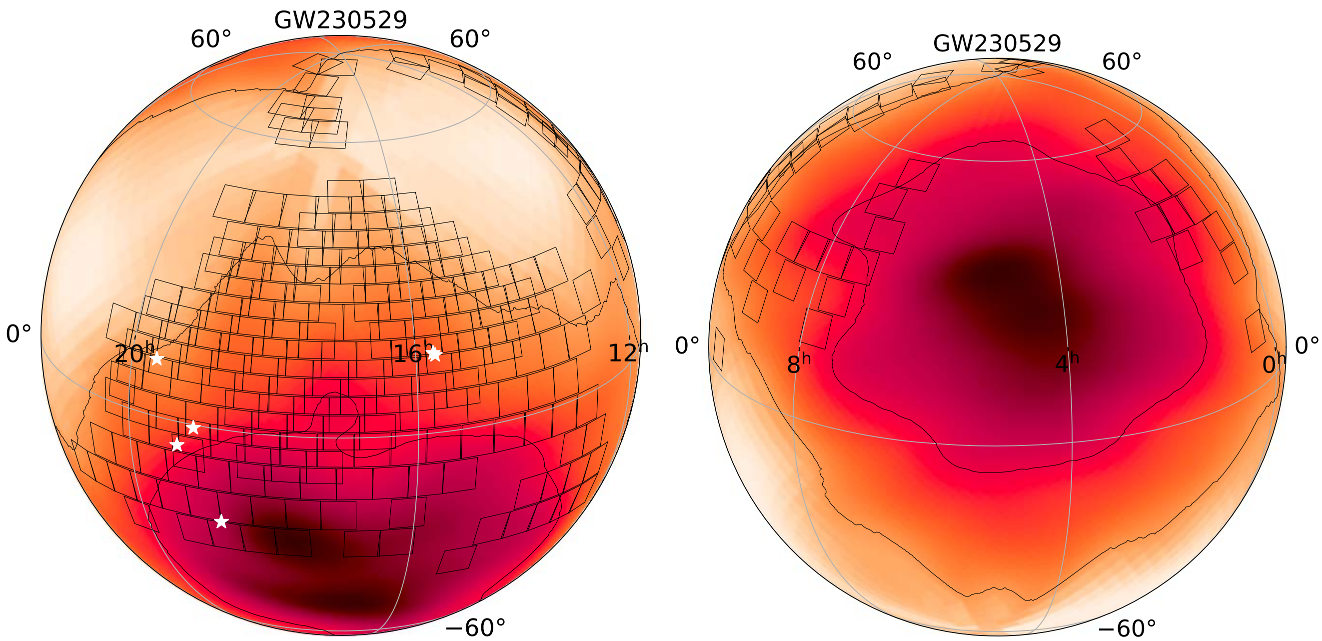

Figure 6. Localization of the high-significance event GW230529, overplotted with the ZTF tiles and the 90% probability contour.

likely NSBH (86%) and its 90% credible region spanned close to 460 deg^2. The majority of the region was observable only from the Southern hemisphere, and ZTF covered ∼2% of the initial region. However, IGWN circulated an updated localization 8 days after the event for which the ZTF coverage was negligible.

4.2. GW230529

GW230529 is a highly significant (FAR of 1 per 160 yr), single detector (LIGO Livingston) event (Ligo Scientific Collaboration et al. 2023b). It was confirmed as an astrophysical event in 2024 April 5th (The LIGO Scientific Collaboration et al. 2024). The 90% credible region spans over 24,000 deg^2, thus we did not trigger ToO observations and decided to re-weight the ZTF survey fields. The first observation started ∼10 hr after the GW trigger and based on the first night, the median limiting magnitudes were $g = 21.1$ and $r = 21.0$ mag. Over three nights of observations, we covered 2425 deg^2, that translates to 7% of the localization region (see Figure 6). We originally found six candidates in this region; upon follow-up, none of them showed KN-like signatures and hence were rejected (Karambelkar et al. 2023). Details of the candidates are presented in Table 3. Although our coverage is only 7%, our limiting magnitudes allow us to set constraints in the properties of the KN, assuming the event was in the ZTF footprint (see Figure 7). Specifically, we can rule out KNe with polar viewing angles ($0^\circ < \theta_{\rm obs} < 26\circ$) within the observed region, assuming a distance of 105 Mpc (corresponding to the median -1σ distance) for the NSBH merger (see Figure 7). The KN brightness in these models decreases monotonically from a face-on (low angles) to an edge-on (high angles) view. KNe viewed from high angles are fainter and therefore more difficult to rule out (see middle and right panel of Figure 7).

4.3. S230627c

S230627c, with a FAR of about 1 in 100 yr, was classified by the `pycbc` (Nitz et al. 2018) pipeline as a likely NSBH (∼50%) or BBH (∼50%) with a relatively small localization: the 90% of the probability spanned ∼82 deg^2 (Ligo Scientific Collaboration et al. 2023c). Even though the `GSTLAL` (Cannon et al. 2021) pipeline classified this event as a BBH (100%), we triggered a targeted search with ZTF. The observations started about 2.2 hr after the GW event and covered 74% (∼72 deg^2) of the skymap (see Figure 8). After an initial inspection of the candidates (Table 3), we ran forced photometry on archival ZTF data, leading to 10 potential counterparts (Anumarlapudi et al. 2023). Further monitoring did not reveal color or magnitude evolution consistent with known KN models or an AT2017gfo-like transient. Observations over the first night reached median magnitude limits of $g = 21.0$ and $r = 21.2$ mag (Ahumada et al. 2023a).

4.4. S230731an

S230731an, had a FAR of a 1 per 100 yr and the 90% credible region of its initial localization covered 599 deg^2 (Ligo Scientific Collaboration et al. 2023d). It was originally detected by the `pycbc` pipeline with a NSBH probability of 18% (BBH

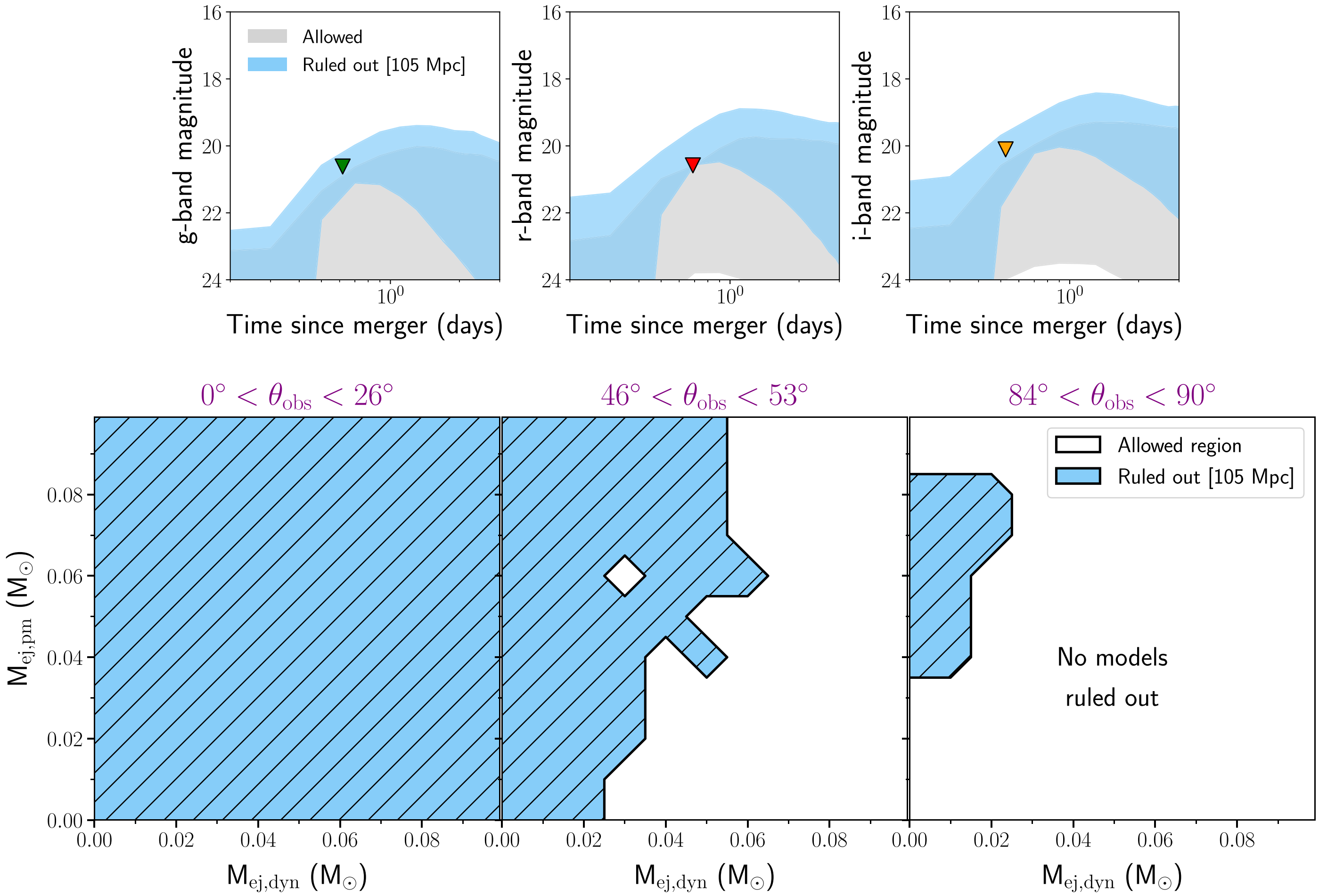

Figure 7. Constraints on KN model parameters based on the ZTF limiting magnitudes on GW230529. Top panels. The g (left), r (middle) and i (right) band median upper limits are shown as green, red, and yellow triangles, respectively, together with NSBH KN models: the blue area encompasses light curves that are ruled out by the limits at 105 Mpc (corresponding to median distance minus 1σ distance uncertainties from LIGO), while the gray area encompasses light curves that are compatible with the limits. These NSBH-specific models are computed with `POSSIS` (Bulla 2019; Anand et al. 2020) and have three free parameters: the mass of the lanthanide-rich dynamical ejecta ($M_{ej,dyn}$), the mass of the post-merger disk-wind ejecta ($M_{ej,pm}$) and the viewing angle (θ_{jobs}). Due to the diverse evolution of the light curves (e.g., some decay faster than others), an overlap between the allowed light curves and the ruled-out light curves produces a darker shade of blue. Bottom panels. Regions of the $M_{ej,pm}$–$M_{ej,dyn}$ parameter space that are ruled out at 105 Mpc and for different viewing angle (θ_{jobs}) ranges (from a face-on to an edge-on view of the system from left to right), assuming the KN fell within the ZTF footprint. Exclusion regions are found for all viewing angles, but here we show those at polar (0–26 deg), intermediate (46–53 deg) and equatorial (84–90 deg). We note the white diamond in the lower-middle panel is due to numerical noise in the simulations, with the r-band limit being slightly brighter than the ($M_{ej,dyn}$, $M_{ej,wind}$) = (0.03,0.06) M_{Sun} model while slightly fainter for neighboring models.

probability of 81%), while the `gstlal` pipeline classified it as a probable BBH (99%). Due to its large inferred distance of 1001 ± 242 Mpc, we decided to re-weight the ZTF fields. Due to weather, the ZTF coverage was ∼3% (43 deg^2), reaching a depth of $g = 18.7$ mag, and no candidates were found in the region in a 72 hr window (see Figure 9).

4.5. S231113bw

Detected by `pycbc`, this event had a relatively moderate FAR of about 1 per 2.35 yr, and was initially classified as a likely BBH (79%), or a NSBH (17%) (Ligo Scientific Collaboration et al. 2023e). Offline analyses by IGWN later classified this event as a likely BBH (96%), and lowered the probability of it being an NSBH to less than 1%. The 90% credible region spanned ∼1713 deg^2, and although it was mostly a northern hemisphere event, the majority of the error region was in close proximity to the Sun. We covered about 11% of the skymap (301 deg^2, see Figure 10), achieving a depth of $g = 21.17$ mag, and found no candidates that passed our filters (Ahumada et al. 2023d).

5. Discussion

In this section, we quantify the efficiency of the ZTF searches during O4a, while also including in the analysis the

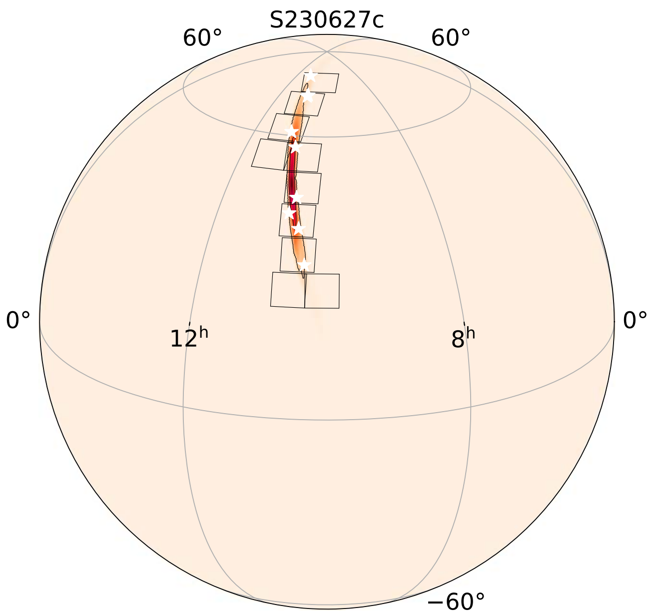

Figure 8. Localization of S230627c, overplotted with the ZTF coverage (black squares) and the 90% probability contour. We show the candidates associated to this event as white stars in the localization region. The rest of the skymaps can be found in the Appendix B, in Figures 6, 9, 10, 18–21.

confirmed astrophysical events from O3. We address this by taking both a Bayesian (Section 5.1) and a frequentist approach (Section 5.2). We use the ZTF observations to constrain the KN luminosity function under different assumptions.

5.1. *nimbus*

In our analysis of the events described above, we have utilized the hierarchical Bayesian framework `nimbus` (Mohite et al. 2022). Briefly, `nimbus` uses a single "average-band" linear model (we will hereafter refer to this model as the Tophat model) for the time evolution of the absolute magnitude using $M(t) = M_0 + \alpha\ (t - t_0)$, where M_0 is the initial magnitude and α is the evolution rate, to determine the likelihood of obtaining the upper limits from ZTF observations given a model (M_0, α). The "average-band" model enables us to use ZTF observations across all bands. In order for `nimbus` to infer the intrinsic luminosity parameters, it requires information about the survey observations, which in this case includes the ZTF observation logs with the specific fields targeted, the Milky Way extinction values for each pointing, and a 3D GW skymap.

`nimbus` determines the posterior probability of a KN with a particular model (in this case, with a specific M_0 and α) given the ZTF observations within the GW skymap. The framework self-consistently accounts for the probability of a GW event being of astrophysical origin ($p_{\rm astro}$) and also factors in the ZTF coverage within the GW skymap. For every sample in the KN parameter space, `nimbus` calculates the likelihood of obtaining the observed limiting magnitude in the ZTF survey, given the model parameters for every field independently. For this, `nimbus` follows Mohite et al. (2022, Section 2.2). We have adopted a uniform distribution for the model priors, and flattened the `multiorder` skymap fits file for all the events to an `nside` of 256. Once the likelihoods have been determined of the observations for each event in all the corresponding ZTF fields, the overall posterior probability of the KN model parameters is determined as in Mohite et al. (2022, Equation (18)).

The combined posterior probability for KN model parameters using events followed up by ZTF during O4a is shown in Figure 11. Based on the ZTF observations of O4a events, `nimbus` shows a preference for models that are fainter than $M_0 = -16$ mag (at a credible level of 0.9), regardless of evolution rate. The yellow shaded regions in Figure 11 correspond to portions of the KN parameter space that ZTF is unable to constrain based on event distances and ZTF upper limits. On the other hand, for fading KNe in the $-16 < M_0 < -19$ mag range, ZTF is partially sensitive, hence the posterior probability has some support for those models (at a credible level of 0.64). The bright KNe that show a rising behavior have the least preference in `nimbus`, with posterior probabilities less than 0.3. We note that the most constraining event is S230627c, as it has the best combination of coverage and depth, while for other events these numbers are more marginal.

5.2. *Simsurvey*

Similarly to previous optical wide field of view (FoV) studies (Kasliwal et al. 2020; Ahumada et al. 2022), we make use of `simsurvey` to estimate the efficiency of the ZTF searches. The strategy that `simsurvey` takes starts with injecting KN-like light-curves in the GW localization volume, then uses the empirical ZTF coverage to measure the KN recovery rate (number of detected KNe divided by the number of injected KNe). We refer to this KN recovery rate as the KN efficiency. `simsurvey` also has filtering functionality, which we use to mimic our realistic candidate filtering criteria. In particular, for KNe to pass the filtering criteria in `simsurvey`, they must have at least two ZTF detections separated by 15 minutes above 5σ. We run separate simulations within the skymaps of each of the 5 GW events listed in Table 1 as well as the five surviving O3 candidates for which we conducted ZTF follow-up (GW190425, GW190426, GW190814, GW200105 and GW200115). We chose to include GW190814 despite its ambiguous classification, since it remains unclear whether the merger was a BBH or NSBH. We inject three different sets of KN models into `simsurvey`:

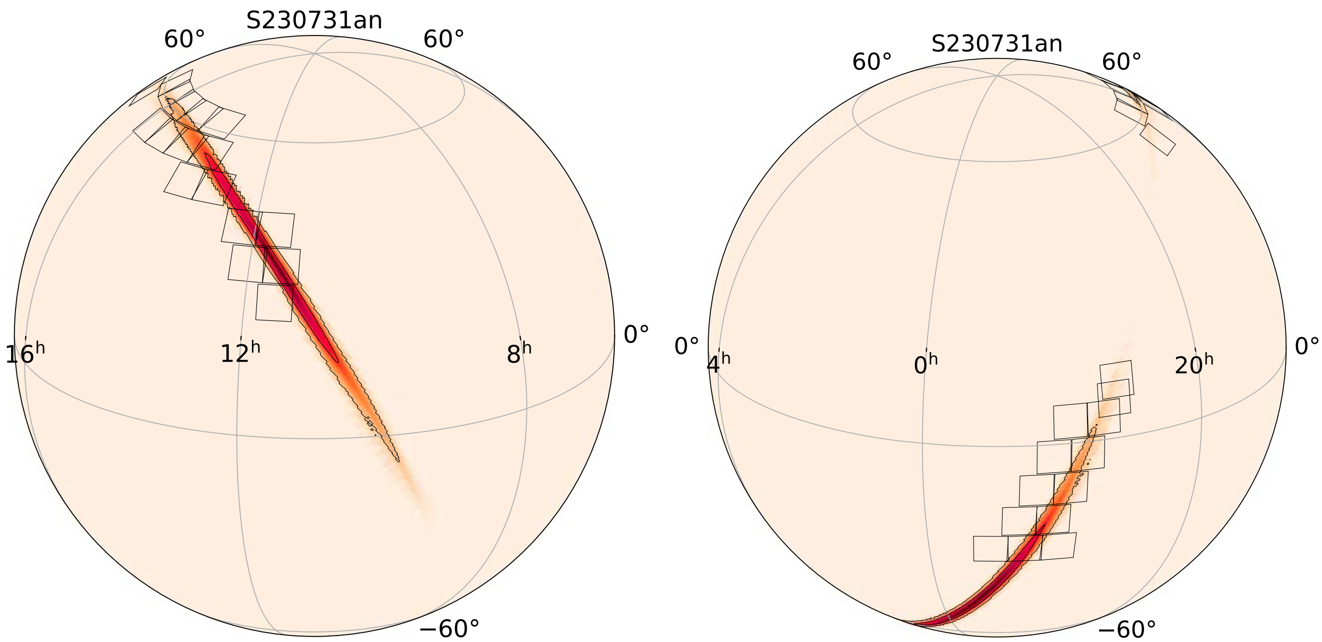

Figure 9. Localization of the high-significance event S230731an, overplotted with the ZTF tiles and the 90% probability contour. We show the candidates discovered in the region as white stars. We note that even though we covered ∼2500 deg^2, the total enclosed probability is only 7%.

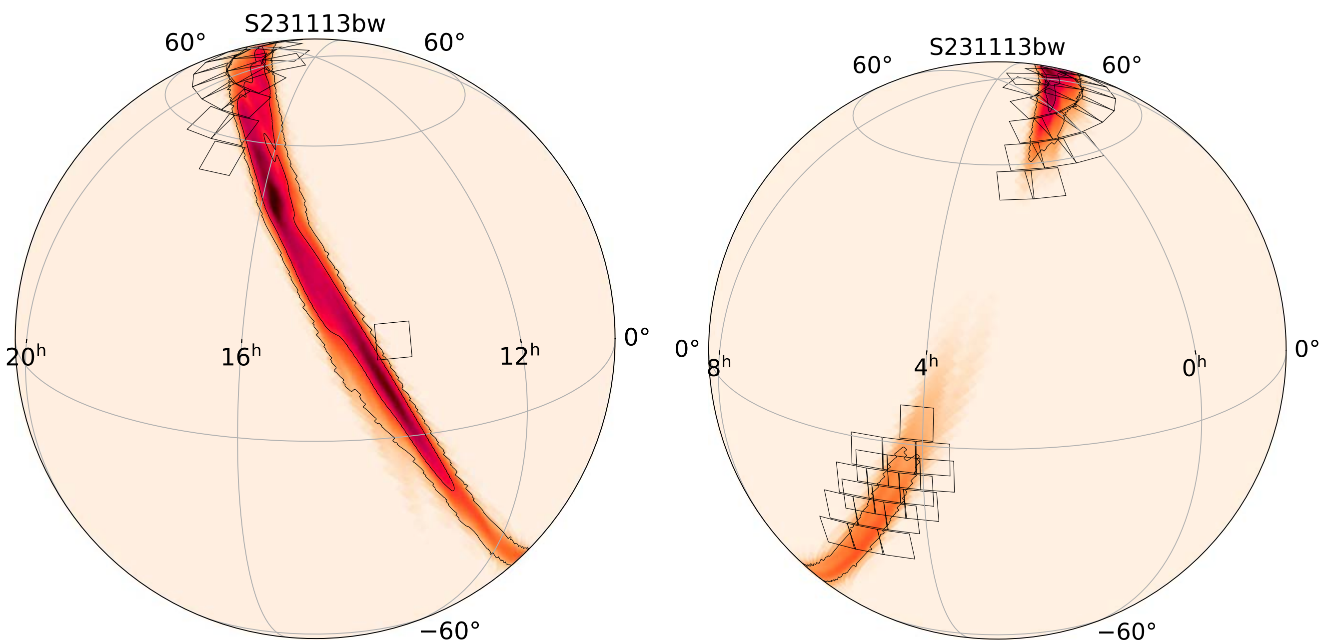

Figure 10. Localization of the high-significance event S231113bw, over plotted with the ZTF tiles and the 90% probability contour. No candidates were found in this region.

1. *Tophat*—an empirical KN model parameterized by initial absolute magnitude (M_0) and evolution rate (α). This same model was used in the `nimbus` framework.
2. POSSIS—the 3D, radiative transfer *Bu2019lm* KN models described in Bulla (2019) and Dietrich et al. (2020), parameterized by dynamical ejecta mass, disk wind ejecta

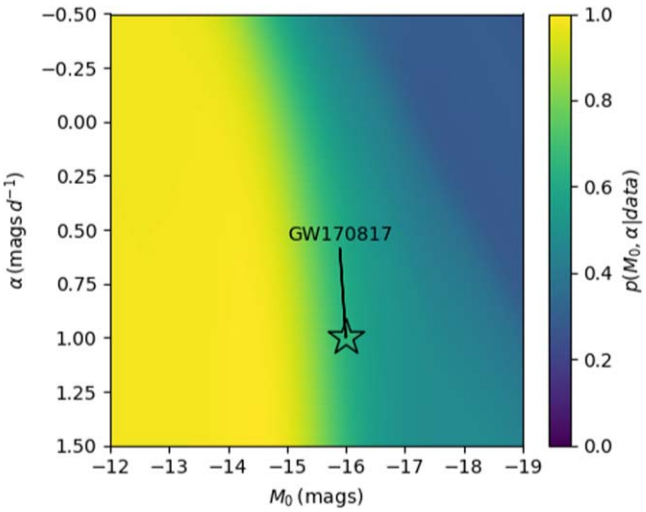

Figure 11. The `nimbus` results of the combined posterior probability for KN model parameters assuming the Tophat model using events followed up by ZTF only during O4a. The *x*-axis shows the initial absolute magnitude M_0 of a model, while the *y*-axis shows its evolution rate α. The color bar shows the posterior probability of each model, in the combined data set, where yellow regions show the favored regions of parameter space given the non-detection of KNe from ZTF observations, and the bluer regions show less preferred combinations for initial M_0 and α. We also mark the position of the average *r*-band decay rate for a GW170817-like KN over its first 3 days of evolution.

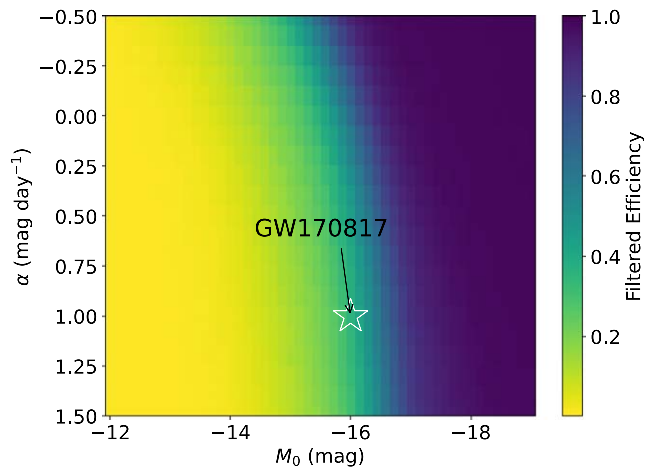

Figure 12. Filtered kilonova efficiency with `simsurvey` for the *Tophat* model evolution. The filtering cuts we apply include a requirement of a minimum of two detections separated by 15 minutes at 5σ. The color bar shows the fraction of sources detected after the filtering vs. the number of sources ingested in the GW volume for the O3 and O4a combined set of skymaps. Similar to Figure 11, we mark the position of a GW170817-like KN on this plot. For this data set, GW170817 has 36% of efficiency.

mass, half-opening angle of the lanthanide-rich component, and viewing angle.

3. *Kasen*—1D, radiative transfer KN models described in Kasen et al. (2017), parameterized by total ejecta mass, velocity, and lanthanide fraction (no viewing angle dependence).
4. *Banerjee*—1D radiative transfer KN model from Banerjee et al. (2022, 2024), parameterized by the density, total ejecta mass, and lanthanide fraction (no viewing angle dependence).

In Figure 12, we plot the KN efficiency for the *Tophat* model after applying the filtering criteria used in the ZTF searches (i.e., two detections). ZTF would detect a GW170817-like KN with $M_0 \approx -16.0$ mag and $\alpha \approx 1.0$ mag day^{-1} passing the basic filtering criteria with 36% efficiency. In contrast, during O3, our joint detection efficiency (i.e., one detection in `simsurvey`) for a GW170817-like KN was 93% (Kasliwal et al. 2020). The lower joint efficiency for O3+O4a events compared to Kasliwal et al. (2020) can be attributed to the fact that many GW event candidates we followed up in O3 were retracted (Abbott et al. 2023a), and we assess efficiency using more realistic criteria of two detections in `simsurvey` rather than one. In the `simsurvey` simulations, we detect KNe brighter than $M_0 = -17.5$ mag with >90% efficiency, indicating that such bright KNe are unlikely to have existed in our data set.

Next, we determine the efficiency with which we can recover GW170817-like KNe in our ZTF observations for more complex models: POSSIS, *Kasen*, and *Banerjee*. Using the best-fit parameters of GW170817, we find that the filtered combined efficiency is 36% and 35% for the POSSIS and the *Kasen* models respectively. The *Banerjee* models, which assume a lanthanide fraction of $X_{\rm lan} = 0.1$, are slightly more pessimistic, predicting a filtered combined efficiency of 20%. We note that the proximity of results from KN models to the approximated *Tophat* model efficiency of 36% shows that the *Tophat* model is a good initial approximation to the KN evolution. In particular, with the *Tophat* model, we can recover GW170817-like KNe with >15% efficiency only in the follow-ups of GW190425 and S230627c, indicating that our most successful EMGW follow-up campaigns with ZTF during O3 and O4a have been of those two events.

While `nimbus`, a Bayesian approach, and `simsurvey`, a frequentist approach, provide independent information about KNe given the ZTF observations, these frameworks are complementary to one another. `nimbus` provides insight into which KN model parameters are more or less favored, given the ZTF observations, while `simsurvey` allows us to assess the recovery efficiency of KNe with particular model parameters from the ZTF follow-ups. When comparing the two analyses, we note similar overall trends: bright KNe ($M \lesssim -17.5$ mag) that exhibit rising behavior have the highest efficiencies in `simsurvey` and are the least preferred by `nimbus`, while faint, fast-fading KNe with the poorest detection efficiencies in `simsurvey` have the highest support in `nimbus` given the ZTF non-detections.

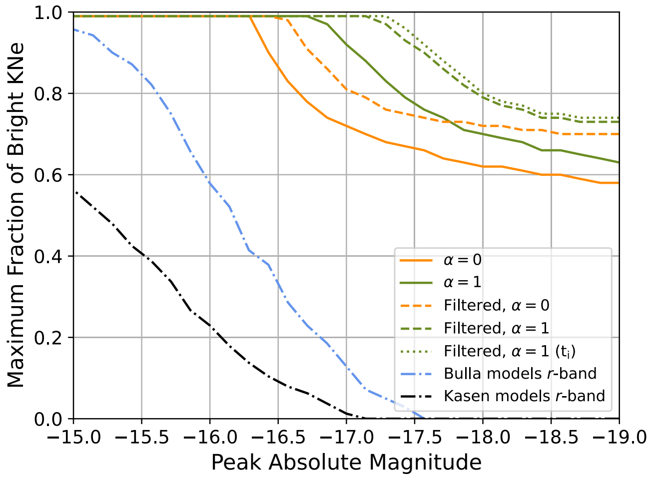

Figure 13. Kilonova luminosity function for events surviving O3, and high significance O4a events. We show in orange the models with flat evolution ($\alpha = 0$), and in green the fading models ($\alpha = 1$ mag day^{-1}. The solid lines show the unfiltered results, while the dashed lines show the results after selecting sources consistent with the ZTF filtering criteria (i.e., two detections). The green dotted line weights models with fading evolution passing the filtering criteria by the event's terrestrial probability (t_i). The black and blue lines show the fraction of Kasen and Bulla models whose peak magnitudes fall within a particular luminosity bin.

5.3. Kilonova Luminosity Function Constraints

Combining all of our EMGW follow-ups in O3 and O4a described above, we follow Kasliwal et al. (2020) in calculating the joint constraints on the KN luminosity function. The luminosity function is given by the following equation:

$$(1 - \mathrm{CL}) = \prod_{i=1}^{N} (1 - f_b \cdot p_\mathrm{i} \cdot (1 - t_\mathrm{i})),$$

where CL is the confidence level, f_b is the maximum allowed fraction of KNe brighter than a given absolute magnitude, i runs through the GW events, p_i is the probability of KN detection within a given GW event skymap, and t_i is the terrestrial probability, defined as $1 - (p_\mathrm{astro})$. We solve for f_b at 90% confidence for each 0.1 mag luminosity bin and plot the results in Figure 13. We include separate luminosity function curves corresponding to KNe with flat evolution and declining at 1 mag day^{-1}, with two tiers of criteria: KNe recovered with a single detection (solid lines), and KNe passing our filtering criteria of two 5σ detections separated by 15 minutes (dashed lines). In all of the curves except for the green dotted line, we set t_i to zero for all events, meaning that we assume that all of the events are astrophysical in those cases.

For reference, we plot curves corresponding to the fraction of POSSIS (*Bu2019lm*) and *Kasen* models peaking at, or brighter than a particular luminosity bin (see Figure 13). The POSSIS models span $M_\mathrm{ej,dyn} = 0.001–0.02\,M_\odot$, $M_\mathrm{ej,wind} = 0.01–0.13 M_\odot$, half-opening angles of the lanthanide rich component $\phi = 15–75$ deg, and viewing angles $\theta = 0–90$ deg; we exclude the POSSIS models with half-opening angles of $\phi = 0$ deg and $\phi = 90$ deg. With our ZTF observations, we can place constraints on the luminosity function for fading KNe with $M \lesssim -16.5$ mag, corresponding to ~35% of the POSSIS *Bu2019lm* grid. The POSSIS models shown here are designed for KNe from BNS (and not NSBH) mergers. We note that though many of the events we followed up have a higher p_NSBH than p_BNS, KNe from NSBH mergers are expected to be similar, but redder and fainter on average, compared to those from BNS mergers (Anand et al. 2020), and hence our ZTF observations would be much less sensitive to NSBH KNe.

We also plot a subset of the *Kasen* model grid consisting of total ejecta masses of $M_\mathrm{ej} = 0.01–0.1\,M_\odot$, velocities of $v_\mathrm{ej} = 0.03–0.3c$, and lanthanide fractions of $X_\mathrm{lan} = 10^{-9}–10^{-1}$, excluding the very faint KN models with low total ejecta masses (with $m_\mathrm{ej} < 0.01\,M_\odot$) (see Figure 13). Approximately 10% of the *Kasen* grid KNe are brighter than $M \lesssim -16.5$ mag, corresponding to the portion of the KN luminosity function our ZTF observations are sensitive to. Here, we choose to include a larger subset of the Bulla and Kasen grid models as compared to Kasliwal et al. (2020); this choice is largely motivated by the fact that our limits are less constraining, and thus we cannot confidently exclude any portion of the KN model space.

We calculate a maximum fraction of 76% for KNe (detected at least once by ZTF) brighter than −17.5 mag and fading at 1 mag day^{-1}. If we take into account only KNe passing ZTF filtering criteria of two detections and fold in the event-by-event terrestrial probability, our maximum fraction of KNe brighter than −17.5 mag and fading at 1 mag day^{-1} becomes 92%. At this point, our observations cannot constrain the maximum fraction of GW170817-like KNe (with $M_\mathrm{peak} = -16.5$ mag, fading at 1 mag day^{-1}). Compared to the 40% fraction found in Kasliwal et al. (2020) for objects brighter than −18.0 mag with flat evolution and no filtering imposed, our constraints are slightly worse (we find a maximum fraction of 62% for the same criteria). Out of the 13 GW events contributing to the luminosity function in Kasliwal et al. (2020), only 5 survived to make it to GWTC-2 and GWTC-3. In addition to these events, we include 5 events from O4a; however among these events, we only triggered ToO observations on S230627c, achieving a skymap coverage >70% (all other O4a events have <15% skymap coverage). Thus many more GW events with >50% ZTF coverage are required in O4b in order to place meaningful constraints on the maximum fraction of GW170817-like KNe.

6. Conclusion

During the first half of IGWN's fourth observing run, O4a, we conducted GW follow-ups of five high significance GW events. In this work, we have reported our revised approach to triggering on GW events, novel `Fritz` machinery for rapidly vetting ZTF candidates found within GW skymaps, and our derived constraints on the properties of KNe.

One of the key developments during O4a is `Fritz`, a `SkyPortal` instance to manage ZTF data and coordinate follow-up. This new capability allowed us to receive the initial GW alert, create an observing plan for ZTF, trigger ZTF observations, display the sources on the GW maps, coordinate follow-up observations for telescopes, vet the candidates, and disseminate our results in an organized fashion. We complemented these searches with offline analyses (`nuzft`, `emgw-cave`, and `ZTFReST`), to leave no stone un-turned in our counterpart searches.

In addition to the ZTF ToO observations, we set in place a novel approach to use the ZTF all-sky survey and observe the GW skymap regions by re-weighting the schedule to maximize the nightly coverage. In total, we conducted observations for 5 high-significance events, and used the re-weighting strategy for 4 of the cases. Only S230518h, S230529ay, S230627c, S230731an, and S231113bw were considered of high significance, as they all had FAR < 1 yr^{-1}, and $p_{\rm BNS} > 0.1$ or $p_{\rm NSBH} > 0.1$ or HasNS > 0.1. We describe in Appendix B the results for the follow-up of additional events with a FAR > 1 yr^{-1}. In summary, we followed-up over 15 ZTF KN candidates and found no viable GW optical counterpart.

Given the ZTF skymap coverages and limiting depths of these GW events, the lack of an associated KN counterpart is consistent with our non-detection analyses. For this, we used both Bayesian and frequentist frameworks. The Bayesian approach, `nimbus`, allows us to compare which combination of parameters are more likely to have been consistent with the non-detections during our O4a campaigns, and gives preference to KN models with starting absolute magnitudes fainter than -16 mag. Our frequentist approach used `simsurvey` to simulate sources in the GW skymap volumes, leading to an overall combined efficiency of 36% for GW170817-like KNe in O3 and O4a. Both analyses show similar trends, with `nimbus` showing a preference for fainter models, and `simsurvey` exhibiting a high recovery efficiency for bright models, painting a cohesive picture between the two frameworks.

The combination of the ZTF observations during O3 and O4a allow us to set constraints on the KN luminosity function. We find that a maximum fraction of 76% of all KNe can be brighter than -17.5 mag. Our results are less constraining than the ones in Kasliwal et al. (2020), mainly due to the number of high-significance events followed up and the ZTF skymap coverage for the events considered. By observing 9 (17) GW events with >90% (50%) coverage to a sensitivity of $M_{\rm peak} > -16$ mag, we would be able to set constraints on the maximum fraction of GW170817-like KNe at the 25% level (Kasliwal et al. 2020).

New near-infrared (NIR) facilities, such as WINTER (Lourie et al. 2020) and PRIME (Kondo et al. 2023), have recently joined the multi-messenger search campaigns. We expect that coordinated efforts in GW searches will lead to the use of these facilities to discriminate candidates based on their NIR evolution, and that they could conduct independent searches for GW events for skymaps in the <500 deg^2 regime. Such well-localized GW events are expected to be routinely detected in O5 (Weizmann Kiendrebeogo et al. 2023). Upcoming wide field surveys, such as the Rubin observatory (Ivezić et al. 2019), ULTRASAT (Shvartzvald et al. 2024), The Nancy Grace Roman Space Telescope, and UVEX (Kulkarni et al. 2021) will open a new window in the GW searches, surveying larger volumes and exploring the UV regime. Wide FoV surveys, such as ZTF, will continue to play a fundamental role in identifying fast fading counterparts that will likely have no previous history in these new data streams.

One of the main challenges we faced during both O3 and O4a was the large localization areas associated with each of the events. We look forward to the second phase of O4, with the re-integration of Virgo to the network of interferometers at an increased sensitivity, which will reduce the sizes of IGWN sky localizations. New events discovered during O4b will likely improve our KN luminosity function constraints, while the verdict on whether the O4a events included in this analysis are recovered in offline GW analysis will also affect the results of this work.

The development of efficient tools to interface with ZTF, such as `Fritz`, has proven to be useful in the broader context of MMA during O4a, and will continue to be a valuable asset to our search efforts during O4b. `Fritz` has allowed multiple astronomers in the same team to analyze the ZTF data stream simultaneously, sharing notes and conclusions about the evolution or behavior of the candidates. `Fritz` also allows for the exploration of new observing strategies using `simsurvey`, as it can determine the KN recovery efficiency given a skymap, distance and latency. The ability to trigger automated follow-up of promising candidates within the Fritz interface itself, and generate ready-to-send GCNs summarizing our follow-up efforts are ways in which we have significantly reduced our latency in the GW follow-up process, increasing our chances of detecting the associated KN.

During O4b, we plan to include ZTF forced photometry throughout the candidate filtering stages, rather than post-facto. This is now possible because of the inclusion of forced photometry in the ZTF alert packets which are also accessible to the broader community. Additionally, new tools such as GWSkyNet may enhance our ability to target candidates that are less likely to be caused or influenced by detector noise by providing an independent metric that can be consistently interpreted across all candidates (Cabero et al. 2020; Abbott et al. 2022; Raza et al. 2024). GWSkyNet annotations are currently expected to be publicly available for LIGO-Virgo events in O4b on GraceDB.[46]

[46] https://emfollow.docs.ligo.org/userguide/content.html#gwskynet-classification

Recent recommendations from the broader EM community (The 2023 Windows on the Universe Workshop White Paper Working Group 2024) underline the importance of prompt, public access to images and alerts, and not just the vetted counterpart candidates, from surveys conducting MMA search campaigns. Our frequent use of the re-weighting strategy during O4a has ensured immediate access to ZTF images and alerts from those GW follow-ups. This approach could be adopted by future surveys, such as the Vera C. Rubin Observatory's Legacy Survey of Space and Time survey. For both ToO and re-weighting follow-ups, we report our pointings (and limiting magnitudes) to the `TreasureMap` as soon as our observations have completed. Furthermore, the development of critical software infrastructure to streamline telescope coordination and efficiency is emphasized in the white paper.

Following these recommendations, we highlight three specific areas where software infrastructure needs to be improved to boost multi-messenger discovery. First, joint querying of heterogeneous discovery streams in real-time (e.g., querying ZTF, WINTER, Rubin and LS4 simultaneously with kowalski) will enable both timely selection of the most promising multi-messenger candidates as well as timely rejection of the false positives. Second, a decentralized communications framework could facilitate active follow-up co-ordination between independent teams. This will enable optimal use of limited follow-up resources that are already the bottleneck in multi-messenger searches (e.g., communication between decentralized SkyPortal instances or similar softwares). Third, incorporating inclination angle constraints into the low-latency GW alert packets could help refine EM counterpart search strategies. For instance, one could tune the targeted depth in optical/IR bands or customize search strategies in radio/high-energy bands based on the expected emission from a KN model with GW inclination constraints applied. Together, such improvements in software infrastructure would amplify the power of collaborative discovery.

Augmenting infrastructure used by the MMA community will make multi-messenger science more accessible to a diverse set of teams around the world. `Fritz` is an example of an open-source tool, catering to the needs of its users, designed to lower the entry barrier for astronomers into time-domain astronomy and MMA. It serves as an intuitive interface to analyze astronomical data, while exploiting the interactive nature of a number of surveys and online catalogs. We look forward to the infrastructure developments that will address the challenges raised by the MMA community, as they will foster a more inclusive approach to enabling MMA discoveries.

Acknowledgments

We thank Fabio Ragosta, Nidhal Guessoum, and Albert K.H. Kong for the useful comments and suggestions. M.M.K., S.A. and T.A. acknowledge generous support from the David and Lucile Packard Foundation. We acknowledge the support from the National Science Foundation GROWTH PIRE grant No. 1545949. M.W.C., B.F.H., A.T., and T.B. acknowledge support from the National Science Foundation with grant Nos. PHY-2308862 and PHY-2117997. This work used Expanse at the San Diego Supercomputer Cluster through allocation AST200029—"Towards a complete catalog of variable sources to support efficient searches for compact binary mergers and their products" from the Advanced Cyberinfrastructure Coordination Ecosystem: Services & Support (ACCESS) program, which is supported by National Science Foundation grants #2138259, #2138286, #2138307, #2137603, and #2138296. C.M.C. acknowledges support from UKRI with grant Nos. ST/X005933/1 and ST/W001934/1. G.C.A. thanks the Indian National Science Academy for support under the INSA Senior Scientist Programme.

Based on observations obtained with the Samuel Oschin Telescope 48 inch and the 60 inch Telescope at the Palomar Observatory as part of the Zwicky Transient Facility project. ZTF is supported by the National Science Foundation under grants No. AST-1440341 and AST-2034437 and a collaboration including current partners Caltech, IPAC, the Oskar Klein Center at Stockholm University, the University of Maryland, University of California, Berkeley, the University of Wisconsin at Milwaukee, University of Warwick, Ruhr University, Cornell University, Northwestern University and Drexel University. Operations are conducted by COO, IPAC, and UW.

SED Machine is based upon work supported by the National Science Foundation under grant No. 1106171.

The ZTF forced-photometry service was funded under the Heising-Simons Foundation grant #12540303 (PI: Graham).

The Gordon and Betty Moore Foundation, through both the Data-Driven Investigator Program and a dedicated grant, provided critical funding for SkyPortal.

This research has made use of the NASA/IPAC Extragalactic Database (NED), which is funded by the National Aeronautics and Space Administration and operated by the California Institute of Technology.

The Liverpool Telescope is operated on the island of La Palma by Liverpool John Moores University in the Spanish Observatorio del Roque de los Muchachos of the Instituto de Astrofisica de Canarias with financial support from the UK Science and Technology Facilities Council.

This work relied on the use of HTCondor via the IGWN Computing Grid hosted at the LIGO Caltech computing clusters.

Appendix A
Observing and Data Reduction Details for Follow-up Observations

A.1. Photometric Follow-up

We show the photometric light-curves of all the candidates in Figures 14, 15, and 16.

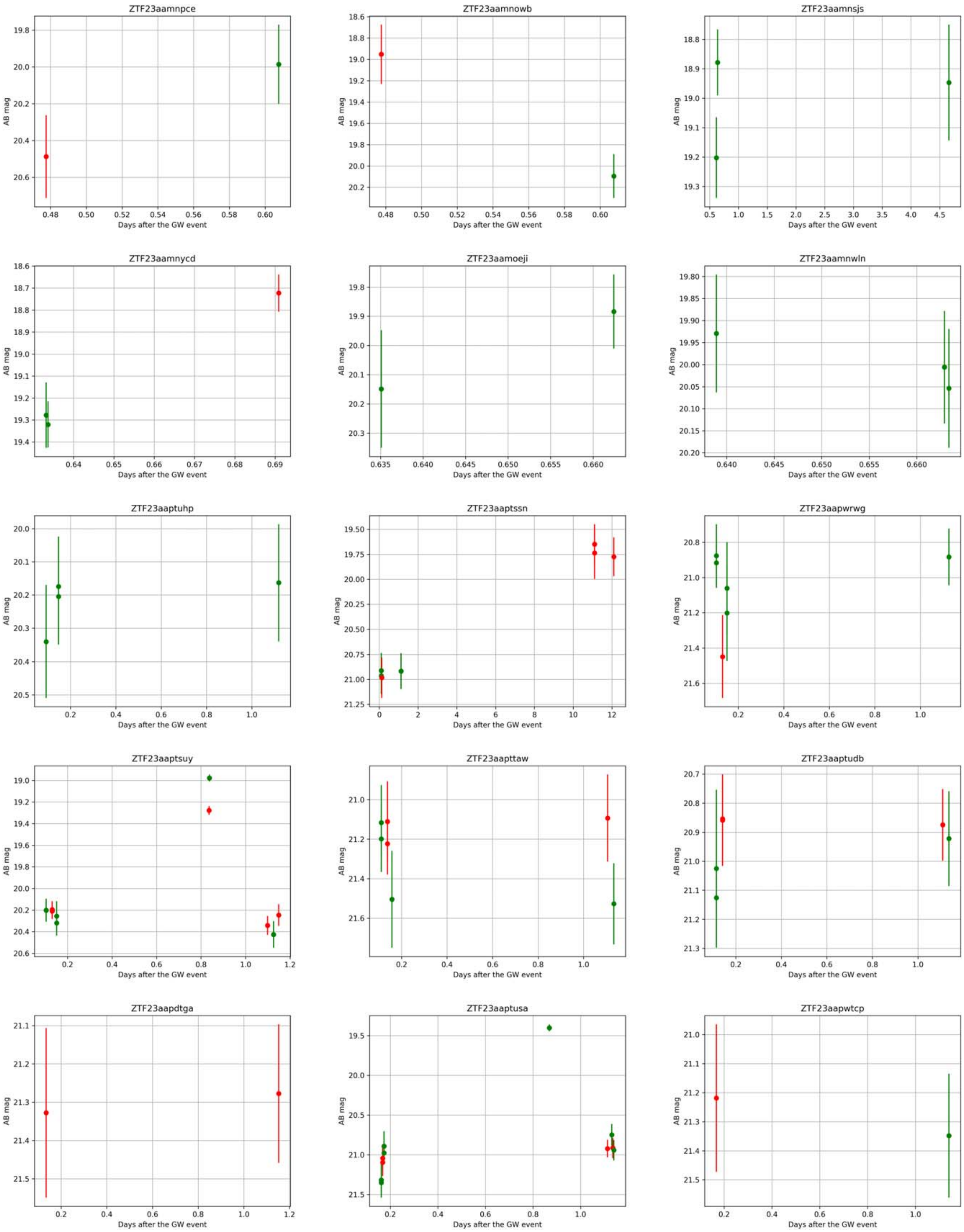

Figure 14. Light-curves for ZTF candidates found during O4a. These candidates correspond to the high-significant events S230529ay and S230627c.

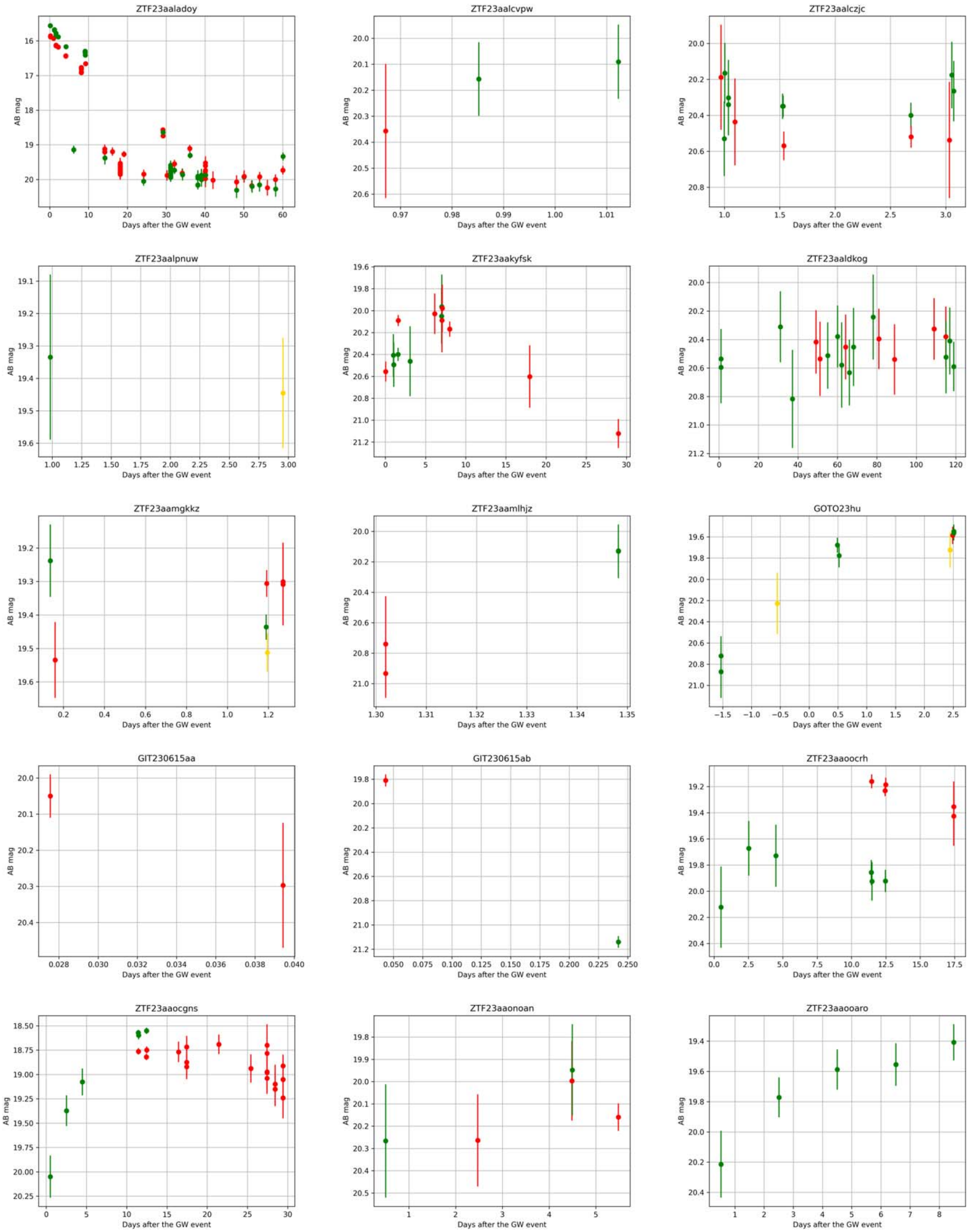

Figure 15. Light-curves for ZTF candidates found during O4a. These candidates correspond to the events S230521k and S230528a.

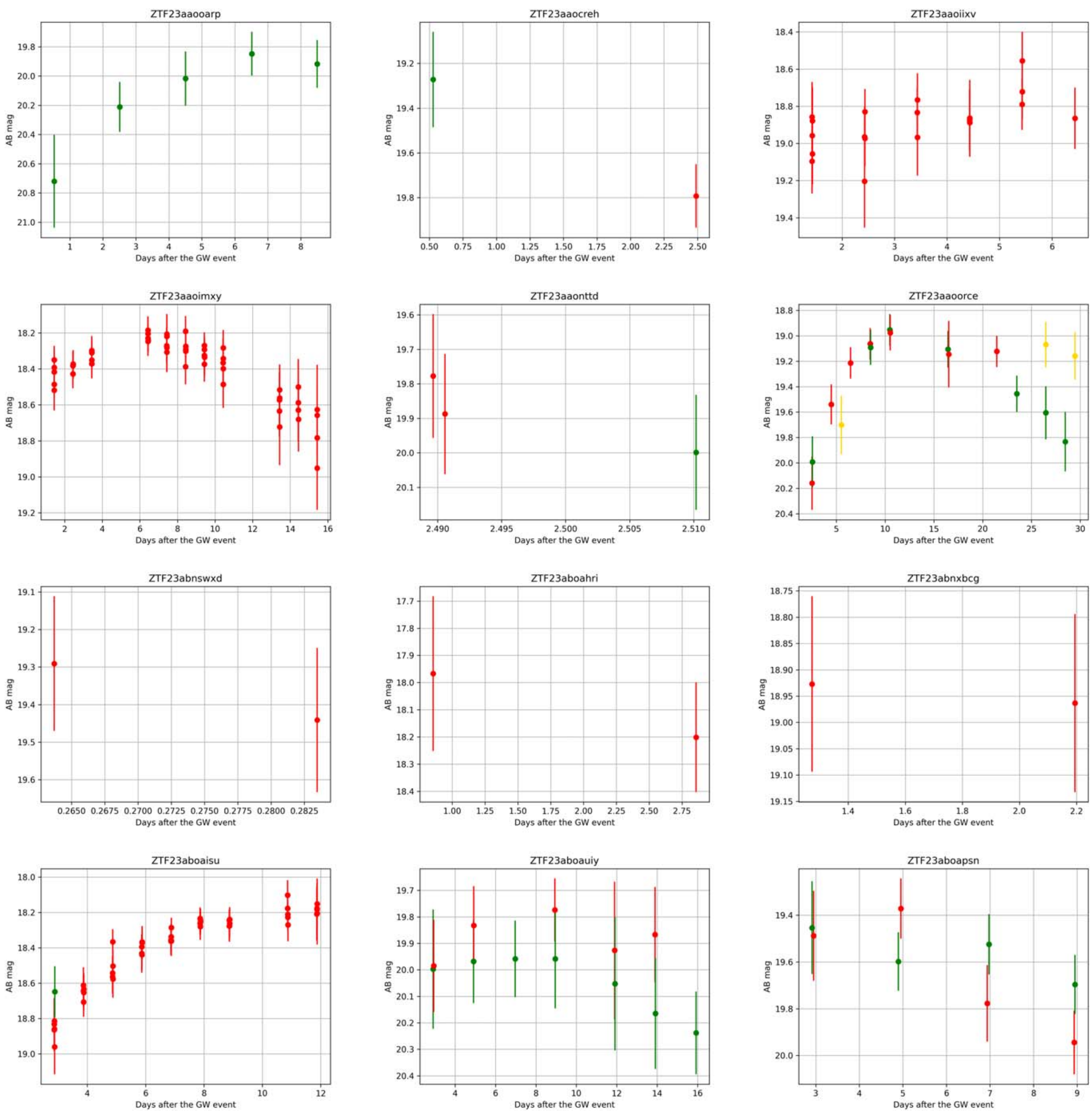

Figure 16. These candidates correspond to the events S230521k S230528a and S231029k.

Palomar 60 inch. We acquired photometric data utilizing the (SEDM; Blagorodnova et al. 2018; Rigault et al. 2019) mounted on the Palomar 60 inch telescope. The SEDM is a low resolution ($R \sim 100$) integral field unit (IFU) spectrometer with a multi- band (*ugri*) Rainbow Camera (RC). The follow-up request process is automated and can be initiated through `Fritz`. Standard requests typically involved 180 s exposures in the *g*-, *r*-, and *i*-bands, however it can be customized and for some transients we used 300 s exposures. The data undergoes reduction using a Python-based pipeline, which applies

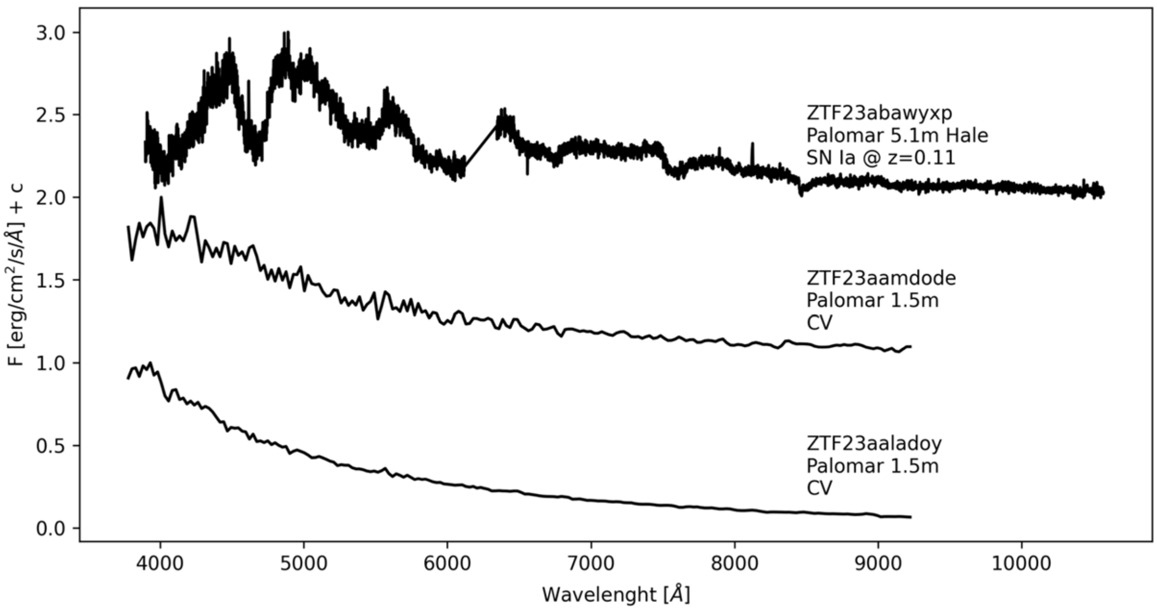

Figure 17. Spectra of the counterpart candidates taken during O4a.

standard reduction techniques and incorporates a customized version of FPipe (Fremling Automated Pipeline; Fremling et al. 2016) for image subtraction.

GROWTH-India Telescope. We utilized the 0.7 m robotic GROWTH-India Telescope (GIT) (Kumar et al. 2022), located in Hanle, Ladakh. It is equipped with a 4k back-illuminated camera that results in a 0.82 deg^2 field of view. Data reduction is performed in real-time using the automated GIT pipeline. Photometric zero points were determined using the Pan-STARRS catalogue, and PSF photometry was conducted with PSFEx (Bertin & Arnouts 2010). In cases where sources exhibited a significant host background, we performed image subtraction using `pyzogy` (Guevel & Hosseinzadeh 2017), based on the ZOGY algorithm (Zackay et al. 2016).

Liverpool Telescope. The images acquired with the Liverpool Telescope (LT) were taken using the IO:O (Steele et al. 2004) camera equipped with the Sloan *griz* filterset. These images underwent reduction through an automated pipeline, including bias subtraction, trimming of overscan regions, and flat fielding. Image subtraction occurred after aligning with a PS1 template, and the final data resulted from the analysis of the subtracted image.

A.2. Spectroscopic Follow-up

Palomar 60 inch. Through `Fritz`, we can assign transients for spectroscopic follow-up with SEDM. The low-resolution ($R \sim 100$) IFU spectrograph is used to charactherize sources brighter than 18.5 mag. The classification is done by running SNID (Blondin & Tonry 2007) and NGSF (Goldwasser et al. 2022) on the reduced spectra (see Figure 17).

Palomar 200 inch. We observed ZTF candidates using the Palomar 200 inch Double Spectrograph (DBSP; Oke & Gunn 1982). The setup configuration involved 1″, 1.″5, and 2″ slitmasks, a D55 dichroic, a blue grating of 600/4000, and a red grating of 316/7500. We applied a custom PyRAF DBSP reduction pipeline (Bellm & Sesar 2016) to process and reduce our data (see Figure 17).

Appendix B
Additional ZTF Triggers

Throughout O4a, ZTF covered the region of events detected with a FAR > 1 yr^{-1}. We triggered observations for S230521k, S230528a, S230615az, S230729cj, and S231029k (See Table 2 for a summary, and Figure 18, 19, 20, and 21 for coverage).

B.1. S230521k

S230521k had a source classification with 25% probability of it being a BNS system and 14% being a NSBH system but had a high FAR of 76 yr^{-1}. S230521k properties did not merit a targeted search, thus we re-weighted the nominal ZTF schedule. The observations spanned a total area of 1294 deg^2, covering 20% of the total probability. The first serendipitous observation was taken around ∼5 minutes after the GW event. The median seeing during the observations is ∼2″, and limiting magnitudes of the first night are $g = 21.37$ and $r = 21.42$ mag. Based on the first two nights of observations, 13 candidates passed our automatic and manual inspection and upon further monitoring, none of them showed any promising nature (Ahumada et al. 2023c; Swain et al. 2023). Details of the

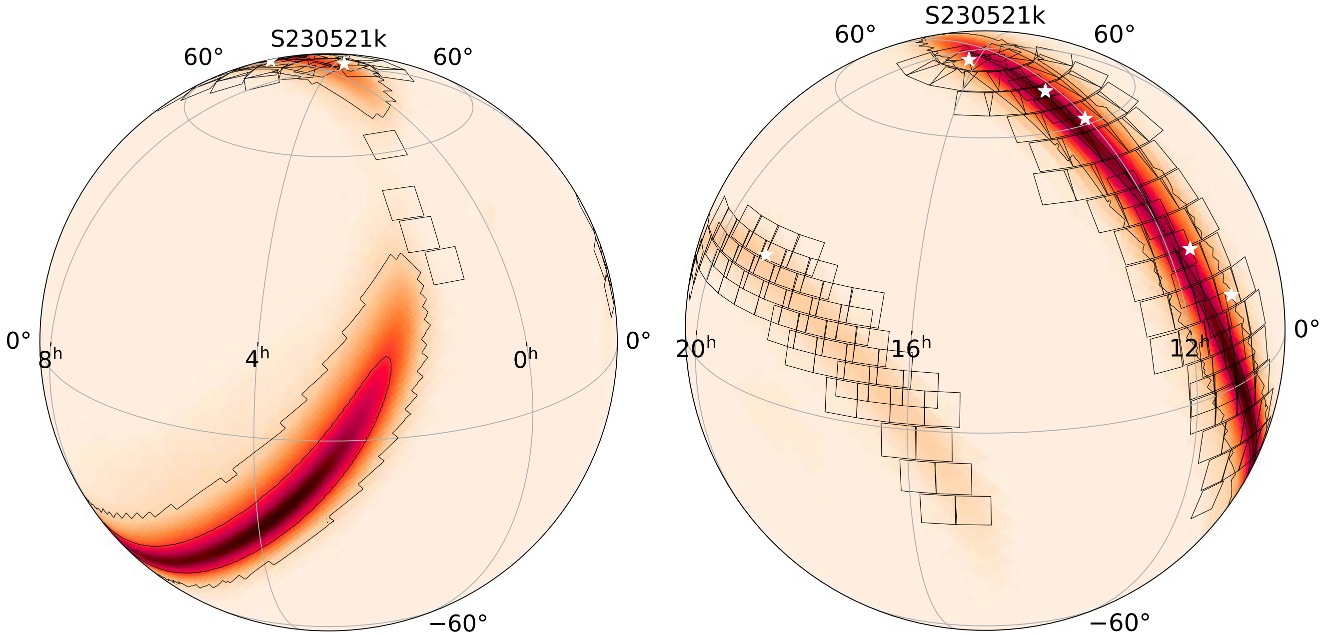

Figure 18. Localization of S230521k, overplotted with the ZTF tiles and the 90% probability contour. We show the cnadidates in the region as white stars.

Table 2
Summary of ZTF Observations and GW Properties for 5 GW Events Additionally Followed-up with ZTF, with FAR > 1 Yr^{-1}

Trigger	Strategy	FAR (yr^{-1})	p_{BNS}	p_{NSBH} prob.	HasNS prob.	HasRemnant prob.	HasMassGap prob.	Distance (Mpc)	Covered prob.	Area covered (**deg^2**)	g-band Depth (AB mag)	Latency (hr)
S230521k	Re-weighting	76	0.25	0.14	1.0	0.9	0.0	454	20%	1294	21.37	0.03
S230528a	Re-weighting	9	0.31	0.62	0.98	0.07	0.73	261	4%	315	20.92	3
S230615az	Re-weighting	4.7	0.85	0.0	1.0	1.0	0.01	260	31%	1063	21.25	11
S230729cj	No coverage	3.82	0.0	0.39	0.0	0.61	1.0	344	0%	…	…	…
S231029k	Re-weighting	93	0.68	0.0	1.0	1.0	0.46	571	36%	6836	19.28	0.23

Note. Similarly to Table 1 we quote other quantities intrinsic to the GW event, such as the mean distance to the merger, the `HasRemnant`, and the `HasMassGap` parameters.

candidates along with the rejection criterion are presented in Table 3.

B.2. S230528a

S230528a was issued with a 40% probability of it being an NSBH system and 20% probability for a BNS system with a FAR of 9 yr^{-1}. Observations included the re-weighting of the ZTF public fields for coverage and the first observation was taken ∼3 hr after the GW alert. The observations during the first two days which covered 315 deg^2 and 4% of the total probability. The median limiting magnitudes for the first night of observations was $g = 20.92$ and $r = 21.09$ mag. During the real-time search, we found four candidates (Ahumada et al. 2023b). However, forced photometry on the archival ZTF data and ATLAS data revealed fainter detections in two candidates that predated the GW event and the other two showed flat evolution inconsistent with the expectations for KN emission, so none of the candidates survived for further follow-up (see Table 3).

B.3. S230615az

S230615az was classified as a probable BNS event with 85% probability and a FAR of ∼four yr^{-1}. The initial 90% probability area covered ∼4400 deg^2. The ZTF strategy for this event relied on the re-weighting of the nominal ZTF fields, covering in total 31% of the region. While most of the probability lied in two southern lobes, ZTF was able to observe ∼1063 deg^2. We found two candidates, but both of them had

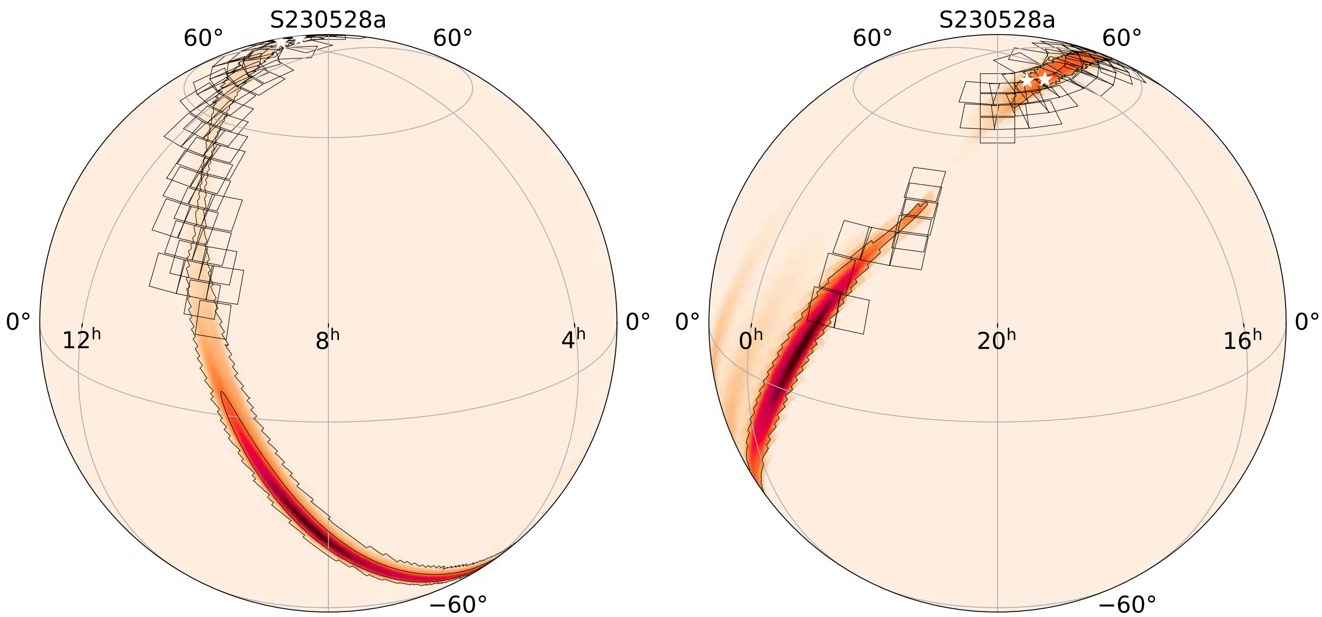

Figure 19. Localization of S230528a, overplotted with the ZTF tiles and the 90% probability contour. We show the transients consistent with KNe candidates as white stars.

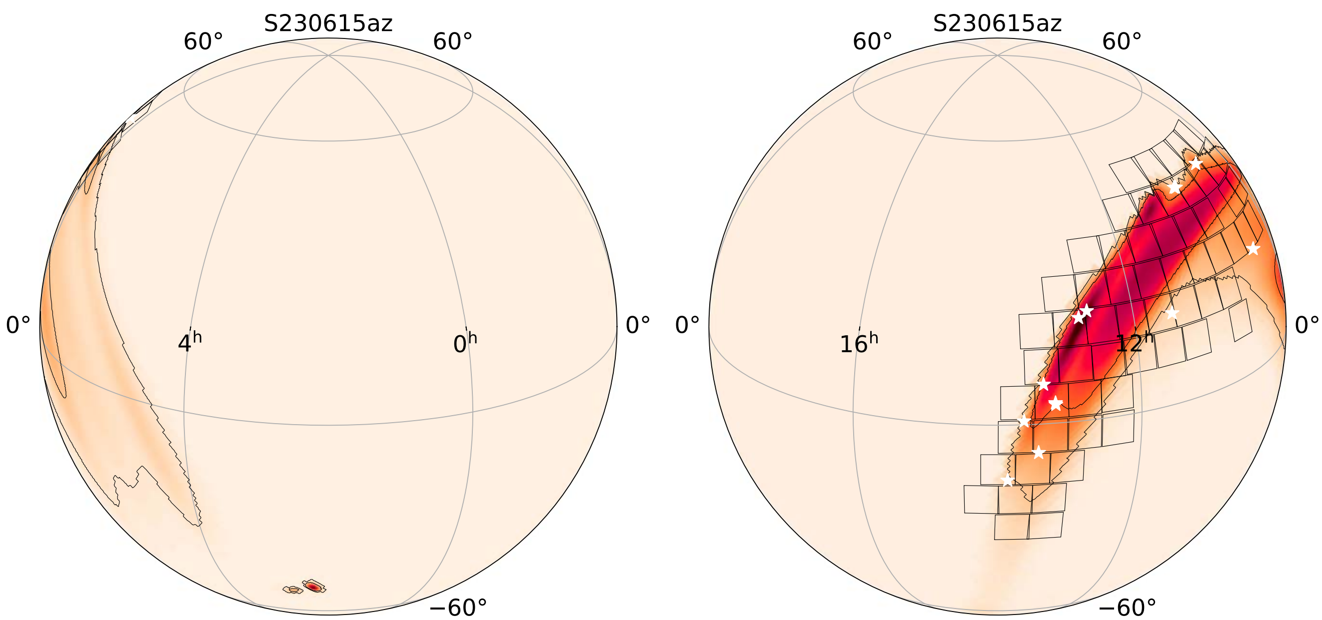

Figure 20. Localization of S230615az, overplotted with the ZTF tiles and the 90% probability contour. We show the candidates as white stars.

pre-detections ∼11 days before the GW trigger. No candidates were selected for further follow-up. Additionally, GOTO found a candidate counterpart to the GW event with an L band magnitude of 19.43 ± 0.08 (Gompertz et al. 2023), but forced photometry on ZTF data revealed that this candidate had a g-band detections 36 hr before the GW trigger and hence we ruled it out (see Table 3 for details). Observations with LBT classified the GOTO transient as a SN Ia (Maiorano et al. 2023). GIT obtained multiple 300 s exposures in the r filter by starting to observe 6 minutes after the GW event, and was able to cover 0.4% of the skymap. GIT found two interesting candidates that passed the cross-checks with Minor Planet Catalog (MPC)—GIT230615aa and GIT230615ab (Kumar et al. 2023). GIT230615aa was later rejected as an interesting

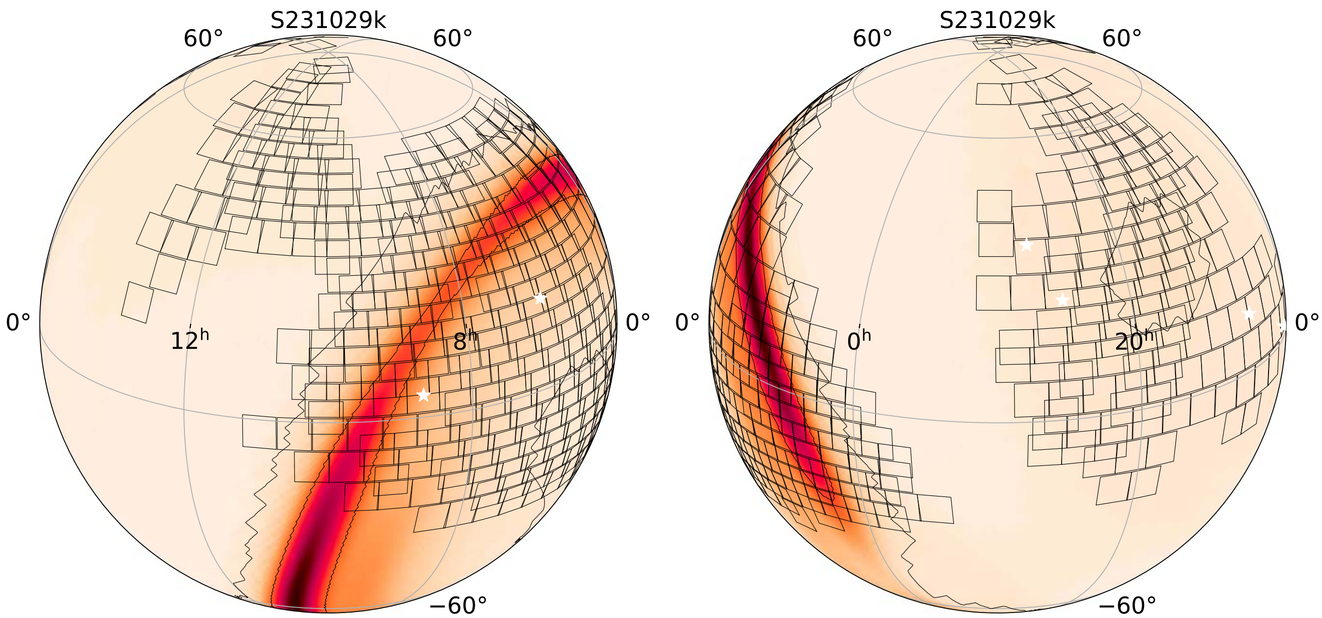

Figure 21. Localization of S231029k, overplotted with the ZTF tiles and the 90% probability contour. We show the candidates as white stars.

Table 3
Properties of the Candidates that Passed Manual Inspection and their Rejection Criteria for Six of the Followed-up LVK Events

Event	Candidate	R.A. [hhmmss]	Decl. [ddmmss]	Discovery Time[a] (hours)	Discovery Mag. (AB magnitude)	Redshift	Rejection Criterion
Candidates for the *High-significance events*: FAR $<$ 1 yr^{-1}							
S230529ay	ZTF23aamnpce	$15^{h}43^{m}56^{s}.1$	$+15^{d}13^{m}29^{s}.3$	11.47	$r = 20.49 \pm 0.23$	0.227	Inconsistent with GW distance
⋯	ZTF23aamnowb	$15^{h}45^{m}31^{s}.2$	$+15^{d}39^{m}03^{s}.5$	11.47	$r = 18.95 \pm 0.28$	⋯	Slow evolution
⋯	ZTF23aamnsjs	$18^{h}40^{m}49^{s}.0$	$-20^{d}39^{m}35^{s}.6$	14.77	$g = 19.20 \pm 0.14$	⋯	Flat evolution
⋯	ZTF23aamnycd	$19^{h}34^{m}57^{s}.5$	$+11d^{d}15^{m}58^{s}.8$	15.21	$g = 19.28 \pm 0.15$	⋯	Slow evolution
⋯	ZTF23aamoeji	$18^{h}57^{m}55^{s}.6$	$-0^{d}37^{m}42^{s}.5$	15.25	$g = 20.15 \pm 0.20$	⋯	Likely galactic
⋯	ZTF23aamnwln	$19^{h}13^{m}03^{s}.8$	$-4^{d}53^{m}51^{s}.1$	15.34	$g = 19.93 \pm 0.13$	⋯	Flat evolution
S230627c	ZTF23aaptuhp	$10^{h}34^{m}41^{s}.1$	$+45^{d}25^{m}31^{s}.3$	2.23	$g = 20.34 \pm 0.17$	⋯	Slow evolution
⋯	ZTF23aaptssn	$10^{h}21^{m}11^{s}.3$	$+31^{d}18^{m}05^{s}.6$	2.41	$g = 20.91 \pm 0.18$	0.15	Slow evolution
⋯	ZTF23aapwrwg	$10^{h}29^{m}03^{s}.6$	$+38^{d}44^{m}34^{s}.6$	2.49	$g = 20.88 \pm 0.18$	0.577	Slow evolution
⋯	ZTF23aaptsuy	$10^{h}40^{m}48^{s}.5$	$+41^{d}58^{m}05^{s}.3$	2.49	$g = 20.2 \pm 0.11$	⋯	Slow evolution
⋯	ZTF23aapttaw	$10^{h}58^{m}45^{s}.5$	$+60^{d}57^{m}16^{s}.4$	2.67	$g = 21.12 \pm 0.19$	0.254	Slow evolution
⋯	ZTF23aaptudb	$11^{h}06^{m}13^{s}.5$	$+78^{d}33^{m}34^{s}.7$	2.75	$g = 21.03 \pm 0.27$	0.188	Slow evolution
⋯	ZTF23aapdtga	$10^{h}46^{m}32^{s}.1$	$+57^{d}08^{m}54^{s}.8$	3.23	$r = 21.33 \pm 0.22$	0.678	Slow evolution
⋯	ZTF23aaptusa	$10^{h}48^{m}10^{s}.6$	$+71^{d}50^{m}29^{s}.1$	3.89	$g = 21.32 \pm 0.2$	0.175	Slow evolution
⋯	ZTF23aapwtcp	$10^{h}49^{m}43^{s}.9$	$+71^{d}24^{m}34^{s}.0$	4.03	$r = 21.22 \pm 0.25$	0.918	Slow evolution
Candidates for the *Other ZTF triggers*: FAR $>$ 1 yr^{-1}							
S230521k	ZTF23aaladoy	$18^{h}40^{m}43.^{s}9$	$+27^{d}01^{m}24^{s}.8$	3.32	$g = 15.56 \pm 0.03$	⋯	Featureless spectrum long-lived (∼200 days).
⋯	ZTF23aalcvpw	$11^{h}33^{m}53^{s}.2$	$+29^{d}11^{m}37^{s}.8$	23.22	$r = 20.36 \pm 0.26$	0.145	Pre-detections
⋯	ZTF23aalczjc	$12^{h}29^{m}02^{s}.8$	$+70^{d}51^{m}01^{s}.8$	23.26	$r = 20.19 \pm 0.29$	⋯	Slow evolution
⋯	ZTF23aakyfsk	$12^{h}03^{m}33^{s}.6$	$+61^{d}23^{m}17^{s}.2$	23.94	$g = 20.41 \pm 0.19$	0.201	Slow evolution
⋯	ZTF23aaldkog	$17^{h}03^{m}21^{s}.3$	$+83^{d}56^{m}32^{s}.9$	24.24	$g = 20.60 \pm 0.25$	⋯	Quasar
S230528a	ZTF23aamgkkz	$17^{h}16^{m}51^{s}.2$	$+75^{d}27^{m}22^{s}.8$	3.27	$g = 19.24 \pm 0.11$	0.105	Slow evolution
⋯	ZTF23aamlhjz	$18^{h}17^{m}47^{s}.0$	$+76^{d}20^{m}35^{s}.1$	31.26	$r = 20.74 \pm 0.31$	⋯	Slow evolution
S230615az	GOTO23hu	$13^{h}22^{m}55^{s}.2$	$+08^{d}09^{m}49^{s}.5$	−36.7	$g = 20.72 \pm 0.19$	⋯	Pre-detections

Table 3
(Continued)

Event	Candidate	R.A. [hhmmss]	Decl. [ddmmss]	Discovery Time[a] (hours)	Discovery Mag. (AB magnitude)	Redshift	Rejection Criterion
⋯	GIT230615aa	$12^h50^m03\overset{s}{.}64$	$+20^d53^m21\overset{s}{.}77$	0.67	$r = 20.05 \pm 0.06$	⋯	Asteroid
⋯	GIT230615ab	$12^h42^m11\overset{s}{.}65$	$+22^d03^m25\overset{s}{.}09$	1.05	$r = 19.81 \pm 0.05$	⋯	Not rejected
⋯	ZTF23aaoocrh	$10^h19^m00\overset{s}{.}1$	$+41^d53^m02\overset{s}{.}8$	11.98	$g = 20.12 \pm 0.31$	⋯	Slow evolution
⋯	ZTF23aaocgns	$10^h17^m01\overset{s}{.}7$	$+41^d44^m38\overset{s}{.}9$	11.98	$g = 20.05 \pm 0.22$	⋯	Slow evolution
⋯	ZTF23aaonoan	$11^h21^m35\overset{s}{.}9$	$+18^d24^m26\overset{s}{.}8$	12.06	$g = 20.27 \pm 0.25$	⋯	Slow evolution
⋯	ZTF23aaooaro	$13^h13^m14\overset{s}{.}5$	$+3^d53^m10\overset{s}{.}4$	12.53	$g = 20.21 \pm 0.22$	0.095	Slow evolution
⋯	ZTF23aaooarp	$13^h13^m29\overset{s}{.}2$	$+4^d13^m31\overset{s}{.}1$	12.53	$g = 20.72 \pm 0.32$	⋯	Slow evolution
⋯	ZTF23aaocreh	$13^h51^m44\overset{s}{.}2$	$-12^d14^m51\overset{s}{.}7$	12.66	$g = 19.27 \pm 0.21$	⋯	Slow evolution
⋯	ZTF23aaoiixv	$9^h06^m17\overset{s}{.}9$	$+22^d29^m45\overset{s}{.}7$	34.23	$r = 18.86 \pm 0.19$	⋯	Slow evolution
⋯	ZTF23aaoimxy	$9^h16^m15\overset{s}{.}1$	$+43^d23^m41\overset{s}{.}3$	34.52	$r = 18.52 \pm 0.11$	⋯	Slow evolution
⋯	ZTF23aaonttd	$13^h27^m02\overset{s}{.}9$	$-6^d10^m06\overset{s}{.}6$	59.76	$r = 19.78 \pm 0.18$	⋯	Slow evolution
⋯	ZTF23aaoorce	$13^h38^m54\overset{s}{.}1$	$+0^d45^m34\overset{s}{.}0$	59.77	$r = 20.16 \pm 0.21$	⋯	Slow evolution
S231029k	ZTF23abnswxd	$6^h37^m33\overset{s}{.}6$	$+18^d16^m39.^s2$	6.34	$r = 19.29 \pm 0.18$	⋯	Slow evolution
⋯	ZTF23aboahri	$16^h24^m19\overset{s}{.}9$	$+1^d43^m55.^s8$	20.51	$r = 17.97 \pm 0.28$	⋯	Slow evolution
⋯	ZTF23abnxbcg	$8^h42^m41\overset{s}{.}8$	$+4^d34^m02.^s2$	30.56	$r = 18.93 \pm 0.17$	0.074	Slow evolution
⋯	ZTF23aboaisu	$17^h48^m33\overset{s}{.}8$	$+11^d34^m10.^s8$	68.79	$r = 18.86 \pm 0.12$	⋯	Slow evolution
⋯	ZTF23aboauiy	$21^h02^m41\overset{s}{.}4$	$+24^d07^m28.^s7$	69.85	$g = 20.0 \pm 0.22$	⋯	Slow evolution
⋯	ZTF23aboapsn	$21^h31^m33\overset{s}{.}2$	$+35^d42^m43.^s5$	69.87	$g = 19.45 \pm 0.2$	⋯	Slow evolution

Notes. There are 15 candidates from the follow-up of *High-significance* events (FAR < 1 yr^{-1}), and 27 candidates for the *Other ZTF triggers* with FAR > 1 $yr^{-1.}$
[a] Time relative to the GW event.

candidate due to deep upper-limits reported (Strausbaugh et al. 2023) soon after the first detection.

B.4. S230729cj

This event had a FAR of 3.8 yr^{-1}, however, the region was almost entirely behind the Sun and the ZTF coverage was of only 2% of the skymap. Hence, we recovered no candidates.

B.5. S231029k

S231029k, with a relatively high FAR of 93 yr^{-1}, was detected by the `spiir` pipeline (Guo et al. 2018) and was initially classified as a likely BNS (68%), with a terrestrial probability of 32%. The 90% credible level of the skymap covered ∼14,968 deg^2, primarily in the southern hemisphere. Our serendipitous observations started about 15 minutes after the GW event and covered about 36% (∼6836 deg^2) of the latest skymap. The first night of observations reached magnitude limits of 19.3 mag in the g band and 19.5 in the r band. No candidates passed our filters.

Appendix C Candidates from ZTF Searches

In this section we summarize all the candidates analyzed during the O4a searches. We include transients not originally detected with ZTF, but later ruled out by us.

Appendix D Regression

We develop a Random Forest (RF) regressor to predict KN properties using low-latency gravitational wave data.

1. We adopt simulations from (Weizmann Kiendrebeogo et al. 2023) as our training data set. This includes 1189 simulated compact binary coalescences that passed detection criteria for O4. The simulations include binary distance, sky position, p-astro, FAR, and an area of 90% sky localization that we include in our features.
2. We compute EM-bright[47] classifications (HasNS, HasRemnant, and HasMassGap) for the simulated data above to include as features.
3. We generate the light curves for each of the simulated events using the nuclear multi-messenger astronomy (NMMA)[48] framework, which relies on the POSSIS model (Bu2019lm; Bulla 2019; Dietrich et al. 2020). We restrict our analysis to simulations with peak magnitudes >18 mag for r filter. We use the peak of the light curve in g and r filters as target.
4. We use the features and target (the information from the GW simulated events and the predicted peak magnitude) to train a RF regressor. To make sure that the scale and measurement units were consistent throughout the training data set, we applied StandardScaler. The data is

[47] https://pypi.org/project/ligo.em-bright/
[48] https://nuclear-multimessenger-astronomy.github.io/nmma/fitting.html

separated into two groups: an 80/20 ratio is used for training and testing, while a 70/30 ratio is used for validation. We obtain an MSE of 0.25 and an R^2 of 0.76 and an MSE of 0.14 and an R^2 of 0.82 in the g-band and r-band for our test data, respectively.
5. For the events included in this paper (see Table 1), we collect the necessary features (FAR, area(90), distance, longitude, latitude, HasNS, HasRemnant, HasMassGap, and P-astro) and use these to predict the peak magnitude using our RF model. The analysis was conducted offline, after the manual candidate vetting was completed.

Our main finding is the estimated peak magnitude for a KN associated with S230627c. Our model predicts a KN peaking at 21.61 mag in the r-band and 22.16 mag in the g-band. According to Table 3, ZTF23aapdtga is 21.80 mag in the g-band and 21.33 mag in the r-band, making this candidate consistent with our predictions within 3σ. No other candidate for any other GW event was within 3σ of the predicted peak.

We expect our RF model to have improved performance with larger and more representative training data, and we look forward to including our predictions to aid in real-time searches.

ORCID iDs

Tomás Ahumada https://orcid.org/0000-0002-2184-6430
Shreya Anand https://orcid.org/0000-0003-3768-7515
Michael W. Coughlin https://orcid.org/0000-0002-8262-2924
Vaidehi Gupta https://orcid.org/0000-0002-7672-0480
Mansi M. Kasliwal https://orcid.org/0000-0002-5619-4938
Viraj R. Karambelkar https://orcid.org/0000-0003-2758-159X
Robert D. Stein https://orcid.org/0000-0003-2434-0387
Gaurav Waratkar https://orcid.org/0000-0003-3630-9440
Vishwajeet Swain https://orcid.org/0000-0002-7942-8477
Theophile Jegou du Laz https://orcid.org/0009-0003-6181-4526
Akash Anumarlapudi https://orcid.org/0000-0002-8935-9882
Igor Andreoni https://orcid.org/0000-0002-8977-1498
Mattia Bulla https://orcid.org/0000-0002-8255-5127
Gokul P. Srinivasaragavan https://orcid.org/0000-0002-6428-2700
Andrew Toivonen https://orcid.org/0009-0008-9546-2035
Avery Wold https://orcid.org/0000-0002-9998-6732
Eric C. Bellm https://orcid.org/0000-0001-8018-5348
S. Bradley Cenko https://orcid.org/0000-0003-1673-970X
David L. Kaplan https://orcid.org/0000-0001-6295-2881
Jesper Sollerman https://orcid.org/0000-0003-1546-6615
Varun Bhalerao https://orcid.org/0000-0002-6112-7609
Daniel Perley https://orcid.org/0000-0001-8472-1996
Anirudh Salgundi https://orcid.org/0000-0003-3173-4691
Aswin Suresh https://orcid.org/0009-0005-8230-030X
K-Ryan Hinds https://orcid.org/0000-0002-0129-806X
Simeon Reusch https://orcid.org/0000-0002-7788-628X
Jannis Necker https://orcid.org/0000-0003-0280-7484
David O. Cook https://orcid.org/0000-0002-6877-7655
Natalya Pletskova https://orcid.org/0009-0008-8062-445X
Leo P. Singer https://orcid.org/0000-0001-9898-5597
Smaranika Banerjee https://orcid.org/0000-0001-6595-2238
Tyler Barna https://orcid.org/0000-0002-4843-345X
Christopher M. Copperwheat https://orcid.org/0000-0001-7983-8698
Brian Healy https://orcid.org/0000-0002-7718-7884
R. Weizmann Kiendrebeogo https://orcid.org/0000-0002-9108-5059
Harsh Kumar https://orcid.org/0000-0003-0871-4641
Ravi Kumar https://orcid.org/0009-0008-6428-7668
Ana Sagués-Carracedo https://orcid.org/0000-0002-3498-2167
Joshua S. Bloom https://orcid.org/0000-0002-7777-216X
Tracy X. Chen https://orcid.org/0000-0001-9152-6224
Matthew Graham https://orcid.org/0000-0002-3168-0139
George Helou https://orcid.org/0000-0003-3367-3415
Russ R. Laher https://orcid.org/0000-0003-2451-5482
Ashish A. Mahabal https://orcid.org/0000-0003-2242-0244
Josiah Purdum https://orcid.org/0000-0003-1227-3738
G. C. Anupama https://orcid.org/0000-0003-3533-7183
Sudhanshu Barway https://orcid.org/0000-0002-3927-5402
Judhajeet Basu https://orcid.org/0000-0001-7570-545X
Dhananjay Raman https://orcid.org/0009-0005-2367-6999
Tamojeet Roychowdhury https://orcid.org/0009-0003-9906-2745

References

Abbott, B. P., Abbott, R., Abbott, T. D., et al. 2017, ApJL, 848, L13
Abbott, B. P., Abbott, R., Abbott, T. D., et al. 2020a, ApJL, 892, L3
Abbott, R, Abbott, T. D., Abraham, S., et al. 2020b, ApJL, 896, L44
Abbott, R., Abbott, T. D., Abraham, S., et al. 2020c, PhRvL, 125, 101102
Abbott, R., Abbott, T. D., Abraham, S., et al. 2021, ApJL, 915, L5
Abbott, R., Abbott, T. D., Acernese, F., et al. 2023a, PhRvX, 13, 041039
Abbott, R., Abbott, T. D., Acernese, F., et al. 2023b, PhRvX, 13, 011048
Abbott, T. C., Buffaz, E., Vieira, N., et al. 2022, ApJ, 927, 232
Abbott, et al. 2017, PhRvL, 119, 161101
Adams, T., Buskulic, D., Germain, V., et al. 2016, CQGra, 33, 175012
Ahumada, T., Anand, S., Coughlin, M. W., et al. 2022, ApJ, 932, 40
Ahumada, T., Andreoni, I., Anumarlapudi, A., et al. 2023a, GCN, 34100, 1
Ahumada, T., Anumarlapudi, A., Karambelkar, V., et al. 2023b, GCN, 33899, 1
Ahumada, T., Karambelkar, V., Stein, R., et al. 2023c, GCN, 33848, 1
Ahumada, T., Salgundi, A., Stein, R., et al. 2023d, GCN, 35032, 1
Ahumada, T., Singer, L. P., Anand, S., et al. 2021, NatAs, 5, 917
Alexander, K. D., Schroeder, G., Paterson, K., et al. 2021, ApJ, 923, 66
Anand, S., Coughlin, M. W., Kasliwal, M. M., et al. 2020, NatAs, 5, 46
Andreoni, I., Coughlin, M. W., Kool, E. C., et al. 2021, ApJ, 918, 63
Andreoni, I., Goldstein, D. A., Anand, S., et al. 2019, ApJL, 881, L16
Andreoni, I., Goldstein, D. A., Kasliwal, M. M., et al. 2020a, ApJ, 890, 131
Andreoni, I., Kool, E. C., Sagués Carracedo, A., et al. 2020b, ApJ, 904, 155
Antier, S., Agayeva, S., Almualla, M., et al. 2020, MNRAS, 497, 5518
Anumarlapudi, A., Ahumada, T., Kasliwal, M., et al. 2023, GCN, 34089, 1

Arcavi, I. 2018, ApJL, 855, L23
Balasubramanian, A., Corsi, A., Mooley, K. P., et al. 2022, ApJ, 938, 12
Banerjee, S., Tanaka, M., Kato, D., & Gaigalas, G. 2024, ApJ, 968, 64
Banerjee, S., Tanaka, M., Kato, D., et al. 2022, ApJ, 934, 117
Bellm, E. C., Kulkarni, S. R., Barlow, T., et al. 2019b, PASP, 131, 068003
Bellm, E. C., Kulkarni, S. R., Graham, M. J., et al. 2019a, PASP, 131, 018002
Bellm, E. C., & Sesar, B. 2016, pyraf-dbsp: Reduction pipeline for the Palomar Double Beam Spectrograph, Astrophysics Source Code Library, ascl:1602.002
Bertin, E., & Arnouts, S. 2010, SExtractor: Source Extractor, Astrophysics Source Code Library, ascl:1010.064
Blagorodnova, N., Neill, J. D., Walters, R., et al. 2018, PASP, 130, 035003
Blondin, S., & Tonry, J. L. 2007, ApJ, 666, 1024
Brown, T. M., Baliber, N., Bianco, F. B., et al. 2013, PASP, 125, 1031
Bulla, M. 2019, MNRAS, 489, 5037
Cabero, M., Mahabal, A., & McIver, J. 2020, ApJL, 904, L9
Cannon, K., Caudill, S., Chan, C., et al. 2021, SoftX, 14, 100680
Chambers, K. C., Magnier, E. A., Metcalfe, N., et al. 2016, arXiv:1612.05560
Chatterjee, D., Ghosh, S., Brady, P. R., et al. 2020, ApJ, 896, 54
Cook, D. O., Kasliwal, M. M., Van Sistine, A., et al. 2019, ApJ, 880, 7
Cook, D. O., Mazzarella, J. M., Helou, G., et al. 2023, ApJS, 268, 14
Coughlin, M. W., Ahumada, T., Cenko, S. B., et al. 2019, PASP, 131, 048001
Coughlin, M. W., Bloom, J. S., Nir, G., et al. 2023, ApJS, 267, 31
Coughlin, M. W., Tao, D., Chan, M. L., et al. 2018, MNRAS, 478, 692
Coulter, D. A., Foley, R. J., Kilpatrick, C. D., et al. 2017, Sci, 358, 1556
de Wet, S., Groot, P. J., Bloemen, S., et al. 2021, A&A, 649, A72
Dekany, R., Smith, R. M., Riddle, R., et al. 2020, PASP, 132, 038001
Dietrich, T., Coughlin, M. W., Pang, P. T. H., et al. 2020, Sci, 370, 1450
Dobie, D., Stewart, A., Hotokezaka, K., et al. 2022, MNRAS, 510, 3794
Drout, M. R., Piro, A. L., Shappee, B. J., et al. 2017, Sci, 358, 1570
Duev, D. A., Mahabal, A., Masci, F. J., et al. 2019, MNRAS, 489, 3582
Evans, P. A., Cenko, S. B., Kennea, J. A., et al. 2017, Sci, 358, 1565
Flesch, E. W. 2023, OJAp, 6, 49
Förster, F., Maureira, J. C., San Martín, J., et al. 2016, ApJ, 832, 155
Fremling, C., Sollerman, J., Taddia, F., et al. 2016, A&A, 593, A68
Goldstein, A., Veres, P., Burns, E., et al. 2017, ApJ, 848, L14
Goldstein, D. A., Andreoni, I., Nugent, P. E., et al. 2019, ApJL, 881, L7
Goldwasser, S., Yaron, O., Sass, A., et al. 2022, TNSAN, 191, 1
Gompertz, B., Kotak, R., Lyman, J., et al. 2023, GCN, 33979, 1
Gompertz, B. P., Cutter, R., Steeghs, D., et al. 2020, MNRAS, 497, 726
Graham, M. J., Kulkarni, S. R., Bellm, E. C., et al. 2019, PASP, 131, 078001
Guevel, D., & Hosseinzadeh, G. 2017, Dguevel/Pyzogy: Initial Release, v0.0.1, Zenodo, doi:10.5281/zenodo.1043973
Guo, X., Chu, Q., Chung, S. K., et al. 2018, CoPhC, 231, 62
Haggard, D., Nynka, M., Ruan, J. J., et al. 2017, ApJL, 848, L25
Hallinan, G., Corsi, A., Mooley, K. P., et al. 2017, Sci, 358, 1579
Hu, Y. D., Fernández-García, E., Caballero-García, M. D., et al. 2023, FrASS, 10, 952887
Ivezić, Ž., Kahn, S. M., Tyson, J. A., et al. 2019, ApJ, 873, 111
Karambelkar, V., Ahumada, T., Stein, R., et al. 2023, GCN, 33900, 1
Kasen, D., Metzger, B., Barnes, J., Quataert, E., & Ramirez-Ruiz, E. 2017, Natur, 551, 80
Kasliwal, M. M., Anand, S., Ahumada, T., et al. 2020, ApJ, 905, 145
Kasliwal, M. M., Cannella, C., Bagdasaryan, A., et al. 2019, PASP, 131, 038003
Kasliwal, M. M., Kasen, D., Lau, R. M., et al. 2022, MNRAS: Letters, 510, L7
Kasliwal, M. M., Nakar, E., Singer, L. P., et al. 2017, Sci, 358, 1559
Kilpatrick, C. D., Coulter, D. A., Arcavi, I., et al. 2021, ApJ, 923, 258
Kim, Y. L., Rigault, M., Neill, J. D., et al. 2022, PASP, 134, 024505
Klimenko, S., Yakushin, I., Mercer, A., & Mitselmakher, G. 2008, CQGra, 25, 114029
Kondo, I., Sumi, T., Koshimoto, N., et al. 2023, AJ, 165, 254
Kulkarni, S. R., Harrison, F. A., Grefenstette, B. W., et al. 2021, arXiv:2111.15608
Kumar, H., Bhalerao, V., Anupama, G. C., et al. 2022, AJ, 164, 90
Kumar, H., Swain, V., Salgundi, A., et al. 2023, GCN, 33974, 1
Levan, A. 2020, PoS, Asterics2, 019, 044
Ligo Scientific Collaboration, VIRGO Collaboration, Kagra Collaboration 2023a, General Coordinates Network, 33813, 1
Ligo Scientific Collaboration, VIRGO Collaboration, Kagra Collaboration 2023b, General Coordinates Network, 33889, 1
Ligo Scientific Collaboration, VIRGO Collaboration, Kagra Collaboration 2023c, General Coordinates Network, 34086, 1
Ligo Scientific Collaboration, VIRGO Collaboration, Kagra Collaboration 2023d, General Coordinates Network, 34303, 1
Ligo Scientific Collaboration, VIRGO Collaboration, Kagra Collaboration 2023e, General Coordinates Network, 35016, 1
Lipunov, V. M., Gorbovskoy, E., Kornilov, V. G., et al. 2017, ApJL, 850, L1
Lourie, N. P., Baker, J. W., Burruss, R. S., et al. 2020, Proc. SPIE, 11447, 114479K
Lundquist, M. J., Paterson, K., Fong, W., et al. 2019, ApJL, 881, L26
Lynch, R., Vitale, S., Essick, R., Katsavounidis, E., & Robinet, F. 2017, PhRvD, 95, 104046
Maiorano, E., Rossi, A., Palazzi, E., et al. 2023, GCN, 34066, 1
Makhathini, S., Mooley, K. P., Brightman, M., et al. 2021, ApJ, 922, 154
Margutti, R., Berger, E., Fong, W., et al. 2017, ApJL, 848, L20
Masci, F. J., Laher, R. R., Rusholme, B., et al. 2019, PASP, 131, 018003
Mohite, S. R., Rajkumar, P., Anand, S., et al. 2022, ApJ, 925, 58
Möller, A., Peloton, J., Ishida, E. E. O., et al. 2020, MNRAS, 501, 3272
Mooley, K. P., Anderson, J., & Lu, W. 2022, Natur, 610, 273
Mooley, K. P., Deller, A. T., Gottlieb, O., et al. 2018, Natur, 561, 355
Morgan, R., Soares-Santos, M., Annis, J., et al. 2020, ApJ, 901, 83
Nitz, A. H., Dal Canton, T., Davis, D., & Reyes, S. 2018, PhRvD, 98, 024050
Nordin, J., Brinnel, V., van Santen, J., et al. 2019, A&A, 631, A147
Oke, J. B., & Gunn, J. E. 1982, PASP, 94, 586
Paek, G. S. H., Im, M., Kim, J., et al. 2024, ApJ, 960, 113
Patterson, M. T., Bellm, E. C., Rusholme, B., et al. 2019, PASP, 131, 018001
Perley, D. A., Ho, A. Y. Q., Fausnaugh, M., et al. 2024, arXiv:2401.16470
Pozanenko, A. S., Barkov, M. V., Minaev, P. Y., et al. 2018, ApJ, 852, L30
Rastinejad, J. C., Paterson, K., Fong, W., et al. 2022, ApJ, 927, 50
Raza, N., Chan, M. L., Haggard, D., et al. 2024, ApJ, 963, 98
Rigault, M., Neill, J. D., Blagorodnova, N., et al. 2019, A&A, 627, A115
Saha, A., Matheson, T., Snodgrass, R., et al. 2014, Proc. SPIE, 9149, 914908
Shappee, B. J., Prieto, J. L., Grupe, D., et al. 2014, ApJ, 788, 48
Shingles, L., Smith, K. W., Young, D. R., et al. 2021, TNSAN, 7, 1
Shvartzvald, Y., Waxman, E., Gal-Yam, A., et al. 2024, ApJ, 964, 74
Singer, L., & Racusin, J. 2023, AAS Meeting Abstracts, 55, 108.02
Singer, L. P., Parazin, B., Coughlin, M. W., et al. 2022, AJ, 163, 209
Singer, L. P., & Price, L. R. 2016, PhRvD, 93, 024013
Smith, K. W., Williams, R. D., Young, D. R., et al. 2019, RNAAS, 3, 26
Soares-Santos, M., Holz, D., Annis, J., Chornock, R., & Herner, K. 2017, ApJL., 848, L16
Srinivasaragavan, G. P., Swain, V., O'Connor, B., et al. 2024, ApJL, 960, L18
Steele, I. A., Smith, R. J., Rees, P. C., et al. 2004, Proc. SPIE, 5489, 679
Stein, R., Reusch, S., Franckowiak, A., et al. 2023, MNRAS, 521, 5046
Stein, R., Reusch, S., & Necker, J. 2023, Zenodo, doi:10.5281/zenodo.7990902
Strausbaugh, R., Pyshna, O., Du Laz, T., et al. 2023, GCN, 34020, 1
Swain, V., Kumar, H., Karambelkar, V., et al. 2023, GCN, 33858, 1
Tachibana, & Miller 2018, PASP, 130, 128001
Thakur, A. L., Dichiara, S., Troja, E., et al. 2021, MNRAS, 501, 2821
The 2023 Windows on the Universe Workshop White Paper Working Group 2024, arXiv:2401.02063
The LIGO Scientific Collaboration, Virgo Collaboration, the KAGRA Collaboration 2024, arXiv:2404.04248
Tiwari, V., Fairhurst, S., & Hannam, M. 2018, ApJ, 868, 140
Tonry, J. L., Denneau, L., Heinze, A. N., et al. 2018, PASP, 130, 064505
Troja, E., Piro, L., van Eerten, H., et al. 2017, Natur, 551, 71
Tucker, D. L., Wiesner, M. P., Allam, S. S., et al. 2022, ApJ, 929, 115
Utsumi, Y., Tanaka, M., Tominaga, N., et al. 2017, PASJ, 69, 101
Valenti, S., David, J. S., Yang, S., et al. 2017, ApJ, 848, L24
van der Walt, S., Crellin-Quick, A., & Bloom, J. 2019, JOSS, 4, 1247
Vieira, N., Ruan, J. J., Haggard, D., et al. 2020, ApJ, 895, 96
Weizmann Kiendrebeogo, R., Farah, A. M., Foley, E. M., et al. 2023, ApJ, 958, 21
Wright, E. L., Eisenhardt, P. R. M., Mainzer, A. K., et al. 2010, AJ, 140, 1868
Wyatt, S. D., Tohuvavohu, A., Arcavi, I., et al. 2020, ApJ, 894, 127
Yao, Y., De, K., Kasliwal, M. M., et al. 2020, ApJ, 900, 24
Zackay, B., Ofek, E. O., & Gal-Yam, A. 2016, ApJ, 830, 27